MATERIALS CHEMISTRY









REVIEW



Cite this: Mater. Chem. Front., 2022, 6, 280

Received 15th September 2021, Accepted 3rd December 2021

DOI: 10.1039/d1gm01267c

rsc.li/frontiers-materials

Cation-intercalation and conversion-type cathode materials for rechargeable aluminum batteries

Tianming Liu, Guocheng Lv, *b Meng Liu, Changchun Zhao, *b *a Libing Liao, *b b Hao Liu, Da Jiayan Shi, Jian Zhang and Juchen Guo **cd

The current research on cation-intercalation and conversion-type cathode materials for rechargeable aluminum batteries (RABs) is discussed in this critical review. The experimental evidence for Al3+ intercalation in transition metal oxides, chalcogenides, MXene, and Prussian blue analogues in both chloroaluminate ionic liquids and aqueous electrolytes is analyzed to identify the true reaction mechanisms. Chevrel phase molybdenum sulfide (Mo₆S₈) is the only proven intercalation material for RABs with unambiguous evidence, different understandings of the Al3+ intercalation mechanism in Mo_6S_8 are discussed. For conversion-type cathode materials, the discussion is focused on the conversion mechanism of metal chalcogenides, and the unique reversible oxidation mechanism of sulfur and selenium enabled by the chloroaluminate ionic liquid electrolytes. The reaction mechanisms of organic cathode materials are also discussed.

1. Introduction

Rechargeable aluminum (Al) batteries are considered as an alternative electrochemical energy storage technology for large-scale applications. Despite the low battery voltage due to the high reduction potential of Al $(-1.7 \text{ V} \text{ vs. SHE})^2$, the high theoretical energy (8046 mA h cm⁻³ and 2981 mA h g⁻¹), low cost, and high abundance of Al make rechargeable Al batteries (RABs) worth investigating.^{4,5} The majority of the research activities on RABs has been focused on cathode materials, which can be categorized into three groups based on different reaction mechanisms: AlCl₄ intercalation materials, Al³⁺ intercalation materials, and conversion-type materials. AlCl₄ is the Lewis neutral anion in the benchmark chloroaluminate ionic liquid electrolytes for RABs. It can reversibly intercalate into graphitic carbon materials with excellent rate capability and cycle stability. To date, the AlCl₄ intercalation cathode materials are overwhelmingly carbon materials including graphite, fewlayer graphene, and reduced graphene oxide. The Al3+ cationintercalation and conversion-type cathode materials include a

2. Al³⁺ intercalation cathode materials

The intercalation cathode materials can host Al3+ cations in their crystal lattice via reversible electrochemical intercalation, and the host lattice must sustain a stable crystal structure.

wide variety of materials, of which most are inspired by their application as electrode materials in lithium-ion (Li-ion) batteries. Although the ionic size of Al³⁺ (0.39 Å) is smaller than that of Li⁺ (0.59 Å), one can expect much more difficult Al³⁺ intercalation due to the large charge density of trivalent Al³⁺ cations. The potential and extent of the conversion reactions in RABs can also be very different from those in Li-ion batteries due to the higher redox potential of Al3+/Al. Furthermore, for either Al³⁺ intercalation or conversion, the active species in the electrolyte are complex chloraluminite anions, which have distinctly different reaction mechanisms from monovalent cations such as Li⁺. In recent years, numerous investigations have been devoted to Al³⁺ intercalation or conversion-type cathode materials for performance improvement and mechanism analysis. However, certain discrepancies still exist in the current literature and the mechanisms were not always rigorously validated. This review provides a comprehensive overview of the reported intercalation and conversion-type RAB cathode materials with emphasis on the clarification of reaction mechanisms. It is worth noting that the intercalation-type and conversion-type materials in this review are categorized based on the claims in the publications, not necessarily reflecting their true mechanisms as discussed below.

 $[^]a$ School of Science, China University of Geosciences, Beijing, 100083, China. E-mail: zhaocc@cugb.edu.cn

^b Beijing Key Laboratory of Materials Utilization of Nonmetallic Minerals and Solid Wastes, National Laboratory of Mineral Materials, School of Materials Science and Technology, China University of Geosciences, Beijing 100083, China. E-mail: guochenglv@cugb.edu.cn

^c Department of Chemical and Environmental Engineering, University of California, Riverside, California, 92521, USA. E-mail: jguo@engr.ucr.edu

^d Materials Science and Engineering Program, University of California, Riverside, California, 92521, USA

A unique challenge for Al³⁺ intercalation is the strong coulombic interaction between the trivalent Al3+ cation and the anionic framework of the host structure. Theoretical calculations indicated that it would be extremely difficult if not impossible for Al³⁺ to intercalate in transition metal oxides or sulfides.⁷ Nevertheless, transition metal oxides, $^{8-13}$ chalcogenides, $^{14-18}$ and their carbon-based composites $^{19-24}$ have been reported as Al³⁺ intercalation cathode materials. It must be pointed out that Al³⁺ intercalation in the current chloroaluminate ionic liquid electrolytes involves chloroaluminate anions, since there are no simple Al³⁺ cations existing in these electrolytes.

2.1 Transition metal oxides

The reported intercalation-type transition metal oxide cathodes for RABs include vanadium dioxide (VO₂), vanadium pentoxide (V₂O₅), lithium vanadate (Li₃VO₄), and tin(IV) oxide (SnO₂). Wang et al. studied VO₂ with a metastable monoclinic structure as the host for Al3+ intercalation-extraction based on firstprinciples calculations.8 The authors simulated that Al occupied the interval of the V-O tunnel in the VO6 octahedron, and increased the number of x from 0 to 4 in the $[Al_x(V_4O_8)]$ structure. The crystal structure remained stable when the number of intercalated Al was from 0 to 2. However, when 3 or 4 Al³⁺ were inserted, the excessively strong ionic bond would cause

serious structural distortion and chemical bond cleavage. A capacity of 165 mA h g⁻¹ in the first discharge was experimentally demonstrated, and it is equivalent to a formula of $Al_{0.17}VO_2$. The capacity retention was 116 mA h g^{-1} after 100 cycles between 0.01 and 0.9 V versus Al under 50 mA g⁻¹. Despite the demonstrated performance, unambiguous experimental evidence for the intercalation mechanism was lacking in this study. The X-ray photoelectron spectroscopy (XPS) results indicated the reduction of V⁴⁺ to V³⁺ after discharge. However, the change in valence state of V cannot validate the intercalation mechanism.

Jayaprakash et al. first reported V2O5 nanowire as an Al3+ intercalation cathode for RABs with promising performance.²⁵ However, a later study by Reed and Menke suggested that the battery-like behavior of the Al-V₂O₅ cells could be the result of the electrochemical corrosion of the stainless steel current collector (iron and chromium) in the chloroaluminate ionic liquid electrolyte.²⁶ Nevertheless, a number of studies of V₂O₅ as the RAB cathode material have been reported since. 9,10,12,25-28 Gu et al. attempted to elucidate the intercalation mechanism and the phase transformation induced by Al3+ in V2O5.10 The galvanostatic discharge-charge curves in their study show a stable discharge slope at 0.6 V and a charge slope around 1.0 V versus Al as displayed in Fig. 1a. The XPS indicated that V⁵⁺ was reduced to V⁴⁺ during discharge. V³⁺ was detected during

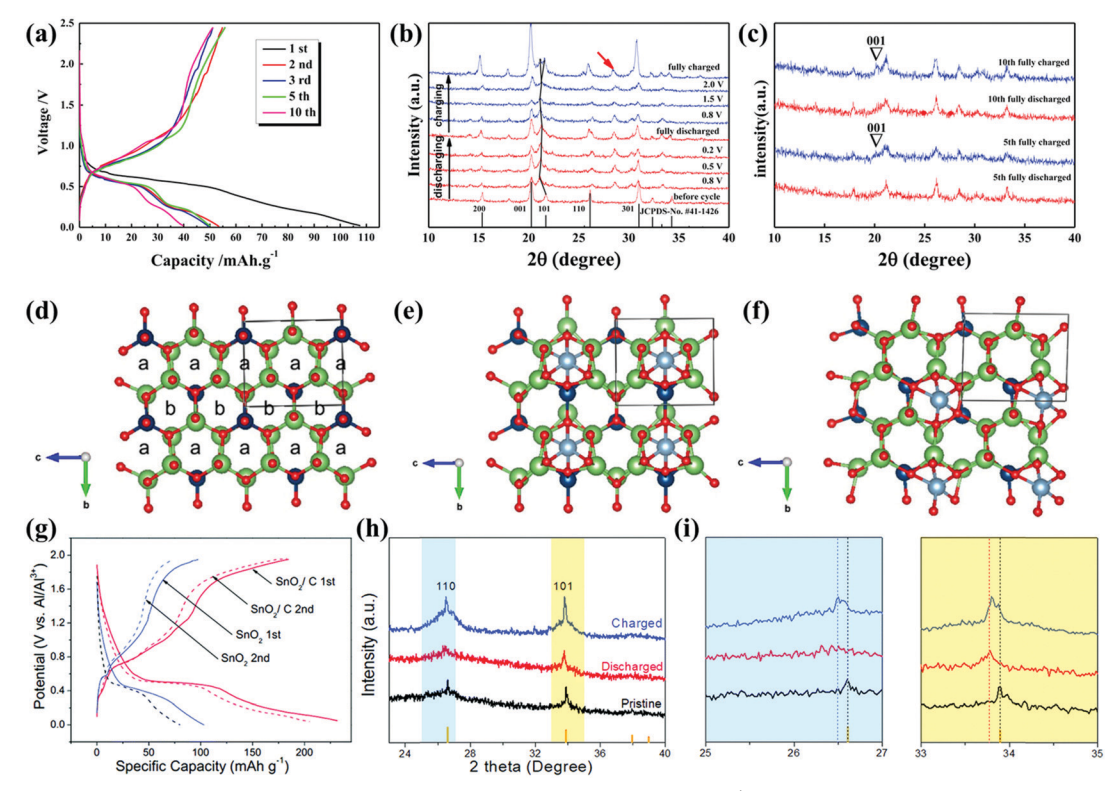


Fig. 1 (a) Galvanostatic charge-discharge curves of V_2O_5 nanowires versus Al under 10 mA g^{-1} ; (b) ex situ XRD of V_2O_5 nanowires during the first cycle at various voltages showing the shift of the (101) peak of orthorhombic V_2O_5 ; (c) ex situ XRD of V_2O_5 nanowires after the 5th cycle and 10th cycle showing the change in the (001) peak attributed to Al intercalation. Reproduced with permission from ref. 10. Copyright (2017) Elsevier. (d) The optimized crystal structure of Li₃VO₄ projected along the a-axis illustrating the a and b sites: Li, green; V, dark blue; O, red; Al, light blue; the structure model of inserting Al into the (e) a site and (f) b site. Reproduced with permission from ref. 11. Copyright (2017) American Chemical Society. (g) The 1st and 2nd dischargecharge potential profiles of SnO_2 and SnO_2/C at 500 mA g^{-1} ; (h) ex situ XRD of SnO_2/C at different stages; (i) enlarged XRD pattern from (h) showing the shift of the (110) and (101) planes. Reproduced with permission from ref. 13. Copyright (2019) The Royal Society of Chemistry.

the charging process, and it was attributed to the disproportionation. The authors also utilized ex situ X-ray diffraction (XRD) to characterize V2O5 at different stages during discharging and charging (Fig. 1b and c). The XRD results showed a shift of the (101) peak and changes in the (001) peak of the orthorhombic V₂O₅, which was interpreted as the reversible structural change induced by the Al³⁺ intercalation. However, discrepancies were presented in the study: the galvanostatic intermittent titration technique (GITT) was used to measure the near-equilibrium discharge and charge potentials. The results showed that the equilibrium potentials of discharge (intercalation) and charge (extraction) changed drastically during cycling. This observation suggests that the structure of V₂O₅ was significantly altered by cycling, which is inconsistent with the intercalation mechanism. The transmission electron microscopic (TEM) characterization revealed an amorphous layer on V₂O₅ after discharge, indicating an irreversible structural change in V₂O₅. Finally, the use of nickel (Ni) foam as the current collector is questionable. Shi et al. demonstrated that Ni is not stable in the chloroaluminate ionic liquid electrolyte, and the discharge-charge behavior in the Al-Ni cell can be obtained due to the corrosion reaction to form active nickel chloride (NiCl₂).²⁹ The complexity of the V₂O₅ cathode was further revealed by Wen et al., who studied the chemical compatibility between V2O5 and the chloroaluminate ionic liquids.³⁰ Their results concluded that V₂O₅ chemically reacts to both Lewis neutral AlCl₄ and Lewis acidic Al₂Cl₇ anions to produce V-containing electrochemically active species in the electrolyte. Therefore, the feasibility and true reaction mechanism of V₂O₅ as the RAB cathode requires further clarification.

A Li₃VO₄@C composite was demonstrated as a cathode material for RABs with an initial capacity of 137 mA h g⁻¹ at a current density of 20 mA g^{-1} . 11 Ex situ XRD, XPS, 27 Al nuclear magnetic resonance (NMR), and first-principles calculations were applied to study the Al³⁺ intercalation mechanism in Li₃VO₄. The discharge-charge curves and cyclic voltammogram (CV) clearly indicated redox reactions despite lower coulombic efficiency (CE) in the first cycle. The XPS data indicated that the oxidation state of V was reversibly changed between V⁵⁺ and V⁴⁺ during discharge and charge. Moreover, the XRD analysis of Li₃VO₄ at various stages during the first discharge-charge cycle revealed a reversible structural change that was attributed to Al intercalation and extraction. Two possible sites in the Li₃VO₄ crystal structure that can host Al³⁺ cations were proposed (a-site and b-site shown in Fig. 1d). First-principles calculations indicated that the a-site is more stable for intercalated Al³⁺ cations (Fig. 1e and f), and the crystal structure change from XRD was consistent with the intercalation of Al into the a-site. However, long-term cycling results from XRD clearly indicated deterioration of the crystallinity, resulting in a decreased capacity. Although the results and interpretations of this study are self-consistent, the change in the XRD pattern of Li₃VO₄ during the first cycle, which was the main evidence of Al³⁺ intercalation, was too subtle to be fully convincing. Interestingly, the ²⁷Al NMR spectra indicated that the molar ratio of AlCl₄⁻ to Al₂Cl₇⁻ in the electrolyte changed during discharge and charge,

which is inconsistent with the conventional assumption that the same amount of chloroaluminate anions would be consumed and generated at the opposite electrodes. A plausible explanation was not provided in this study, however, based on the understanding of the reactions between chloroaluminate anions and $V_2O_5^{30}$ it is possible that the vanadate anion VO_4^{3-} can chemically react with AlCl₄⁻ and/or Al₂Cl₇⁻.

Lu et al. reported SnO₂ as a cathode material for RABs. 13 Relatively high specific capacity was demonstrated for both SnO₂ and its carbon-supported composite as shown in Fig. 1g. The CV curves of SnO₂/C show a reduction peak at 0.5 V and an oxidation peak at 0.8 V versus Al, corresponding to the plateau of the galvanostatic discharge and charge curves. XPS spectra show that Sn⁴⁺ was partially converted to Sn²⁺ during discharge, and then oxidized to Sn⁴⁺ after charging. Ex situ XRD patterns show that the diffraction intensity of SnO2 decreased after discharging and recovered after charging, and the (110) and (001) crystal planes shifted to the left about 0.1° after the charge/discharge process, which is attributed to the increase in the interlayer space (Fig. 1h and i). Unfortunately, the crystallographic evidence of Al3+ intercalation was not fully convincing due to the low resolution of the XRD patterns.

Transition metal oxides such as titanium dioxide (TiO₂), ^{31–33} manganese oxides, 34,35 vanadium oxides, 36,37 molybdenum trioxide (MoO₃), ^{38,39} and molybdenum-tantalum oxide ⁴⁰ were also studied as the Al³⁺ intercalation cathodes in RABs based on aqueous electrolytes, which are either AlCl₃, Al trifluoromethanesulfonate (Al(OTf)₃), Al sulfate (Al₂(SO₄)₃), or Al nitrate (Al(NO₃)₃) solutions in water. Although battery-like discharge and charge performance were always demonstrated in these studies, unambiguous evidence of Al intercalation in these transition metal oxides was generally lacking. It is also worth noting that all the aqueous electrolytes used in these studies are very acidic due to the hydronium H₃O⁺ generated from the hydrolysis of the hydrated Al³⁺ cations. Transition metal oxides are known for reversible electrochemical intercalation of protons as demonstrated in the studies of V2O5, 41 TiO2, 42 and MoO₃⁴³ in acidic electrolytes. Therefore, the true mechanisms of transition metal oxide cathodes in aqueous RABs need further scrutiny and clarification.

2.2 Spinel or layered transition metal chalcogenides

Compared to transition metal oxides, the analogous chalcogenides generally have a lower specific capacity and lower potential versus Al. However, they could be better host structures for Al³⁺ intercalation compared to oxides due to their more polarizable anion framework and larger lattice sites. Therefore, spinel and two-dimensional (2D) layered metal chalcogenides are natural selections due to their proven applications as hosts for monovalent and divalent cations.44-52

The general formula of cubic thiospinel is AB_2X_4 (A, B = divalent and trivalent metals, respectively, and X = chalcogen), and the arrangement of X is cubic close packing. The divalent cation is filled in one-eighth of the tetrahedral void, and the trivalent cation is filled in one-half of the octahedral void. Li et al. studied porous Co₃S₄ microspheres from solvothermal

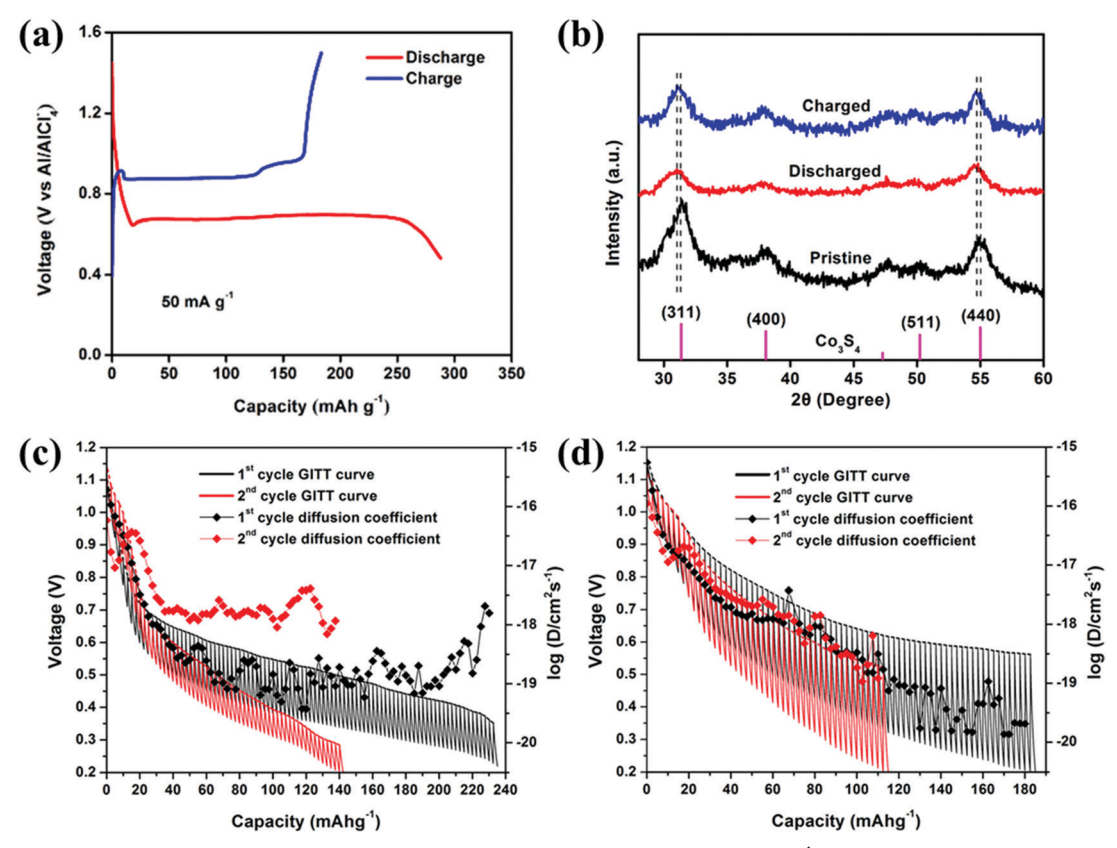


Fig. 2 (a) The first discharge-charge potential curve of Co₃S₄ microspheres versus Al at 50 mA g⁻¹; (b) ex situ XRD patterns of Co₃S₄ at different charging and discharging states. Reproduced with permission from ref. 17. Copyright (2018) Elsevier. The GITT profiles of (c) TiS_2 and (d) $Cu_{0.31}Ti_2S_4$ at 50 °C with a calculated Al³⁺ diffusion coefficient as the function of capacity (i.e., extent of Al intercalation). Reproduced with permission from ref. 15. Copyright (2017) American Chemical Society.

synthesis as the cathode material for RABs. 17 Co atoms occupy both the tetrahedral and octahedral positions in the Co₃S₄ spinel structure. The evaluation of the electrochemical properties of Co₃S₄ was performed with polytetrafluororthylene (PTFE) cells and glassy carbon current collectors to avoid the potential side reactions due to the chloroaluminate ionic liquid electrolyte. The first cycling curve displayed very distinct discharge and charge potential plateaus at 0.68 V and 0.88 V versus Al (Fig. 2a), respectively. Flat potential plateaus in the discharge and charge curves typically indicate phase transformation of the host crystal structure, thus a strong implication of the intercalation mechanism. The CE of the first cycle is only 64%, which was hypothesized as that part of the intercalated Al³⁺ was trapped in the crystal structure due to the strong interaction between Al3+ and the sulfide framework. Furthermore, the XRD pattern showed that the peak intensity of the (311) and (400) planes was reduced and shifted by 0.24° to the left after the first discharge (Fig. 2b), which might be attributed to the Al3+ intercalation. However, due to the low resolution of the XRD patterns before and after discharge, no crystal structural information could be obtained. The distinct plateaus in the discharge-charge curve disappeared after only 5 cycles, indicating that the Co₃S₄ crystal lattice could not sustain a repeated discharge and charge process, thus the phase transformation induced by Al³⁺ intercalation was irreversible. It is interesting that the in situ Raman spectra of the electrolyte indicated the

consumption of the Al₂Cl₇ anion and generation of the AlCl₄ anion after discharge; and vice versa after the charging process. This observation is consistent with the finding in the study by Jiang et al. on Li₃VO₄, ¹¹ again indicating that the chloroaluminate ionic liquid may be actively involved in the RAB reactions.

Geng et al. reported two types of titanium sulfides (thiospinel Cu_{0.31}Ti₂S₄ and layered TiS₂) as Al³⁺ intercalation cathode materials for RABs. 15 The spinel $Cu_{0.31}Ti_2S_4$ has an $Fd\bar{3}m$ space group. Assuming the Cu²⁺ position remains unchanged after discharge, the Rietveld refinement of the XRD patterns suggested that 9% of Al³⁺ occupied the same position as Cu²⁺, resulting in a composition of Al_{0.09}Cu_{0.31}Ti₂S₄. The Rietveld refinement of the XRD pattern of TiS₂ after Al intercalation indicated that the intercalated Al³⁺ cations occupied 11% of the octahedral intercalation position between the TiS₂ layers (Al_{0.11}TiS₂). The unit cell volume of the Al-intercalated TiS2 is reduced, which was attributed to the strong attraction to the TiS₂ layers from the highly charged Al³⁺ cations. The analysis of the GITT discharge at 50 $^{\circ}\text{C}$ showed the diffusion coefficients of Al are 10^{-18} to $10^{-20}~\text{cm}^2~\text{s}^{-1}$ in $\text{Cu}_{0.31}\text{Ti}_2\text{S}_4$ and 10^{-18} to 10^{-19} cm² s⁻¹ in TiS₂ (Fig. 2c and d). The low diffusion coefficient is clearly the main obstacle to the Al intercalation in these two sulfides.

Overall, the layered TiS2 cathode demonstrated a higher reversible capacity than the cubic spinel Cu_{0,31}Ti₂S₄, indicating that the 2D layered structure may be preferable for Al3+

intercalation. To date, a number of other 2D transition metal dichalcogenides including vanadium disulfide (VS₂),²⁰ molybdenum disulfide (MoS₂)²¹ and molybdenum diselenide (MoSe₂)²³ have been reported as cathodes of RABs. Wu et al. reported a nanosheet VS2-graphene composite that exhibited a reduction peak at 0.45 V and an oxidation peak at 1.6 V versus Al in CV as displayed in Fig. 3a. The discharge and charge curves of the VS₂ cathode are slope-like, and the incorporation of graphene improved the capacity and capacity retention (Fig. 3b and c). In situ XRD revealed that the intensity of the (001) and (011) peaks of VS₂ were gradually weakened during discharge until diminished at 0.3 V. After charging to 1.7 V, the diffraction peaks re-appeared. Ex situ XRD indicated that the intensity of the VS2 characteristic peak (001) became lower during the discharge, and slightly shifted to the left, which suggested the layer spacing of (001) was increased. However, the in situ and ex situ XRD analysis is not fully consistent, and the crystallographic data were not distinct enough to draw conclusions on the crystal structure change. Therefore, it is not

clear if the reaction mechanism between Al3+ and VS2 is intercalation.

Yang et al. reported MoS2 as the cathode material for RABs.²¹ The composite composed of MoS₂ and carbon nanofibers (CNFs) showed two pairs of redox peaks (0.55 and 0.8 V of reduction and 1 and 1.15 V of oxidation versus Al) in the CV curve at 0.5 mV s⁻¹, which corresponded well to the plateaus in the discharge-charge curve. The MoS₂/CNFs composite exhibited a good rate performance, and maintained a specific capacity of 112 mA h g^{-1} after 50 cycles at 250 mA g^{-1} (Fig. 3d-f). It is worth noting that the distinct plateaus in the dischargecharge curve are consistent with the intercalation-extraction mechanism. The XPS Mo 3d spectra indicated reversible reduction and oxidation of Mo during discharge and charge. The ex situ XRD also showed that the (002) plane disappeared after full discharge and reappeared when charged to 1.8 V, which was interpreted as evidence of the intercalation mechanism. However, the amount and position of intercalated Al could not be determined due to the low crystallinity of the nanosized MoS₂.

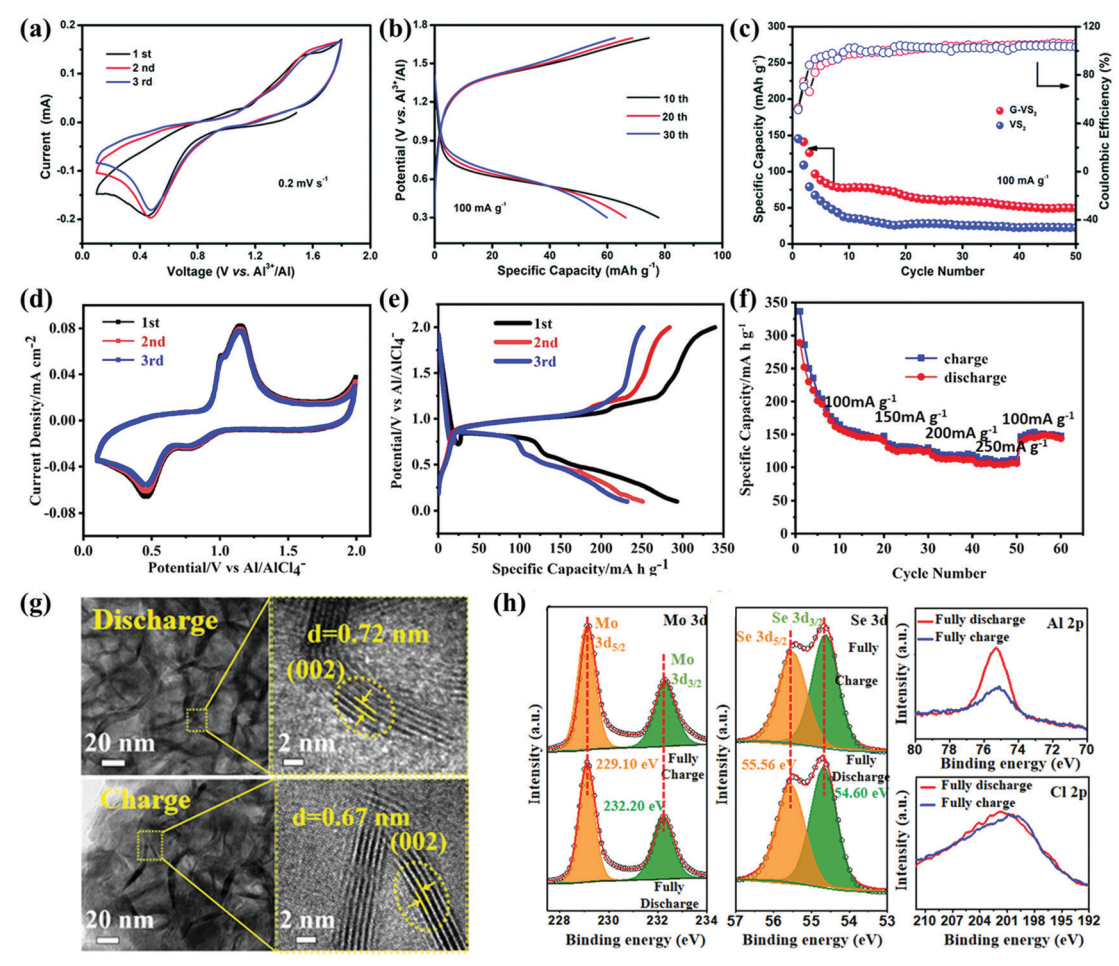


Fig. 3 (a) The CV curves of the VS $_2$ -graphene composite at a scan rate of 0.2 mV s $^{-1}$ versus Al; (b) the 10th, 20th, and 30th discharge-charge curves of the VS $_2$ graphene composite at a current density of 100 mA g^{-1} ; (c) comparison of the cycle stability and CE from VS₂ and VS₂-graphene at 100 mA g^{-1} . Reproduced with permission from ref. 20. Copyright (2018) The Owner Societies. (d) The CV curves of MoS₂/CNFs at a scan rate of 0.5 mV s⁻¹ versus Al; (e) the discharge-charge curves of $MoS_2/CNFs$ at a current density of 100 mA g^{-1} ; (f) rate performance of $MoS_2/CNFs$. Reproduced with permission from ref. 21. Copyright (2019) American Chemical Society. (q) HRTEM images of MoSe₂ after discharge and charge showing the reversible change of the (002) plane spacing; (h) the Mo 3d, Se 3d, Al 2p, and Cl 2p XPS spectra of the fully charged and discharged MoSe₂. Reproduced with permission from ref. 23. Copyright (2021) American Chemical Society.

MoSe₂ was also investigated as the cathode for RABs by An and coworkers.²³ High-resolution transmission electron microscopy (HRTEM) analysis indicated that the d-spacing of MoSe₂ was increased from 6.7 Å to 7.2 Å after full discharge, and it returned to the original state after charging (Fig. 3g). However, the XPS spectra indicated that the oxidation state of Mo was not changed during the discharge and charge (Fig. 3h), which was clearly contradictory to the conventional understanding of the intercalation mechanism. One possible explanation is that selenium (Se) is the active element in MoSe₂ following a conversion mechanism. Interestingly, the Se 3d XPS spectra were not changed either after discharging and charging. This observation suggests that not only was Se active but also soluble species were produced from the electrochemical reaction of Se. The electrochemical activity of Se in metal selenides in chloroaluminate ionic liquids was demonstrated by a number of studies, which will be discussed in the section on conversion-type cathode materials.

2.3 Chevrel phase molybdenum sulfide (Mo₆S₈)

In 2015, Geng et al. first reported Chevrel phase Mo₆S₈ as an Al³⁺ intercalation cathode material for RABs. The Chevrel phase has a unique crystal structure composed of octahedral Mo atoms in the cubic sulfur anion unit cell. There are two positions in the

Mo₆S₈ lattice that can allow intercalation of monovalent and divalent cations. 14,53-58 The first is at the center of the rhombohedron with eight Mo₆S₈ vertices (denoted as Al₁), and the second is a smaller site at the face center of the rhombohedron (denoted as Al2). The CV scan demonstrated two pairs of cathodic/anodic peaks indicating that the two-step electrochemical reaction occurred in the Mo₆S₈ electrode. Consistent with the CV scan, the constant current cycling curves showed two distinct potential plateaus during discharge and two plateaus during charge (Fig. 4a and b), which typically implies an intercalation mechanism. The most unambiguous evidence of Al intercalation came from the XRD of Mo₆S₈ before and after discharge as displayed in Fig. 4c. The XRD pattern after discharge was distinctly different from the pristine Mo₆S₈, and the Rietveld refinement revealed that Al indeed intercalated into the two lattice sites previously mentioned. Following this original study, the same group performed a more detailed study on the phase transformation of Mo₆S₈ induced by Al intercalation. Ex situ XRD was performed at a different stage of Al³⁺ intercalation in Mo₆S₈, and the obtained XRD patterns were analyzed with Rietveld refinement combined with electrochemical and TEM characterizations. 16 The Al 3+ intercalation initially prefers the larger site of Al₁ over the smaller site of Al₂. However, the

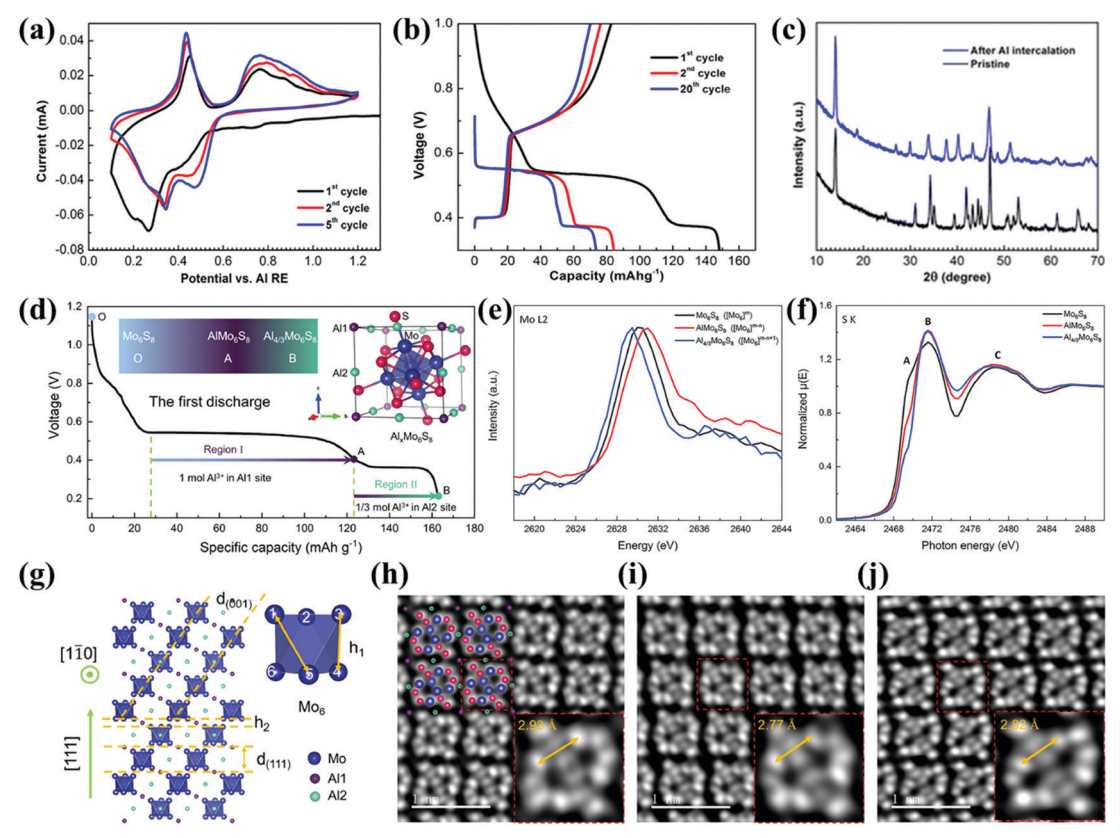


Fig. 4 (a) The CV curves of Mo_6S_8 at $0.1\,\text{mV}\,\text{s}^{-1}$ and $50\,^\circ\text{C}$; (b) the representative discharge–charge curves of Mo_6S_8 at a current density of $12\,\text{mA}\,\text{g}^{-1}$ at 50 °C; (c) XRD patterns of the Mo_6S_8 cathode before and after full discharge. Reproduced with permission from ref. 14. Copyright (2015) American Chemical Society. (d) The first discharge profile of Mo_6S_8 at 10 mA g^{-1} and 55 °C; the insets illustrate the crystal structure of $Al_xMo_6S_8$ and the stages of $Al_xMo_6S_8$ and the stages of $Al_xMo_6S_8$ and $Al_xMo_6S_8$ intercalation; (e) Mo L_2 -edge of EELS spectra; (f) S K-edge of XAS spectra; (g) the crystal structure of Mo_6S_8 along (1 $\overline{10}$) defining the Mo_1 to Mo_5 distance; (h-j) the STEM images of Mo₆S₈, AlMo₆S₈, and Al_{4/3}Mo₆S₈ along (001) showing the bond length of Mo₁-Mo₅ varies with Al intercalation, Mo: blue, S: red, Al₁: purple, Al₂: green. Reproduced with permission from ref. 18. Copyright (2021) Elsevier.

preference quickly diminishes because the strong repulsion between Al³⁺ cations forces the intercalating Al³⁺ cation into the Al₂ sites, resulting in equal occupation in these two sites at the end of the first discharge plateau. During the second discharge plateau, Al3+ cations exclusively intercalate into the larger Al₁ sites due to the strong repulsion between the cations.

Lee et al. proposed a different Al³⁺ intercalation mechanism based on in situ XRD characterization:⁵⁹ Al³⁺ cations intercalate into Mo₆S₈ following a two-step phase change reaction the same as the known Mg^{2+} and Li^+ intercalation in Mo_6S_8 . $^{60-67}$ Al³⁺ cations first exclusively intercalate in the Al₁ site. Once the Al₁ sites are fully occupied resulting in a formula of AlMo₆S₈ at the end of first discharge plateau, the Al3+ cations start to intercalate into the Al2 sites leading to the fully intercalated formula of Al_{4/3}Mo₆S₈. Tong et al. further revealed that the S anions in Mo₆S₈ also undergo a transient redox reaction during Al intercalation and extraction. 18 The two plateaus of the first discharge curve of Mo₆S₈ at 10 mA g⁻¹ and 55 °C contributed 95 mA h g⁻¹ and 35 mA h g⁻¹ capacity respectively, corresponding to 1 mole and 1/3 mole Al3+ intercalation in AlxMo₆S₈ (Fig. 4d). Electron energy loss spectroscopy (EELS) (Fig. 4e) and X-ray absorption spectroscopy (XAS) (Fig. 4f) were used to analyze the change in the valence state of Mo and S during the Al3+ intercalation, respectively. In the pristine Mo_6S_8 , the S^{n-} anion is not in the fully reduced state (0 < n < 2). During the first stage of Al intercalation (Mo_6S_8 to $AlMo_6S_8$), S^{n-} is fully reduced to S^{2-} and simultaneously Mo is oxidized. During the second stage of Al intercalation (AlMo₆S₈ to Al_{4/3}Mo₆S₈), Mo is subsequently reduced meanwhile the valence state of S2- remains unchanged. The synergistic redox of Mo and S is correlated to the change of the crystal structure. The XRD analysis indicates that the interplanar space of (111) decreases after the first Al intercalation (AlMo₆ S_8), and then it increases after further 1/3 Al intercalation (Al_{4/3}Mo₆S₈). The change of the interplanar spacing of (111) can be quantified by the Mo-Mo distance (Mo₁ to Mo₅) in the Mo octahedron as defined in Fig. 4g. The Rietveld refinement of XRD revealed the Mo₁-Mo₅ bond length in Al₁Mo₆S₈ shrinks from the original 2.842 Å to 2.675 Å. When the rest of Al (1/3) was inserted, the bond length increased to 2.709 Å. The change of the Mo₁-Mo₅ bond length was also confirmed by the measurement with scanning transmission electron microscopy (STEM). As displayed in Fig. 4h-j, the Mo_1 - Mo_5 length in the pristine Mo_6S_8 is 2.93 Å, which decreases to 2.77 Å after the first Al intercalation, and then increases to 2.82 Å after further 1/3 Al intercalation.

In addition to the spectroscopic and microscopic techniques described above, solid-state ²⁷Al NMR was also used by Jadhav et al. to analyze the Al3+ intercalation in Mo₆S₈.68 The quantitative ²⁷Al NMR spectra of Mo₆S₈ at different discharge and charge stages indicate simultaneous intercalation of Al3+ into the Al₁ and Al₂ sites. This conclusion is consistent with the finding from Geng et al. from their ex situ XRD study. The solidstate ²⁷Al NMR also revealed the reversible formation of an amorphous layer on the surface of Mo₆S₈, which can be related to the desolvation process of chloroaluminate anions. This is a significant finding since the desolvation (breaking the Al-Cl bonds) prior to Al3+ intercalation has not been understood in

any intercalation-type cathode materials for RABs. It is clear from the studies above that the site occupation dynamics of Al³⁺ intercalation in Mo₆S₈ is still not fully understood to date.

2.4 MXene

MXene is a new group of 2D carbide or nitride materials derived from the mother MAX phase $(M_{n+1}AX_n \text{ where } n = 1 \text{ to } 4, M$ represents early transition metals, A is group 13 or 14 elements, and X is C or N). Typically acidic etching is used to remove the A elements from the MAX phase to obtain MXene with a general formula of $M_{n+1}X_nT_x$, where T represents the surface functional groups such as oxide, fluoride, chloride, and hydroxide resulting from the etching process. 69,70 MXene materials recently attracted tremendous research efforts in applications such as catalysis and electrochemical energy storage. 71,72 Beidaghi and coworkers reported V₂CT_x MXene as an Al-intercalation cathode for RABs. 19 The V₂CT_x MXene is a layered vanadium carbide with many different functional groups on the surface, synthesized by etching Al from the V₂AlC MAX phase. At a current density of 10 mA g⁻¹ within a voltage range of 0.1-1.8 V, the capacity of the 1st discharge is 178 mA h g^{-1} . Ex situ XRD showed weakening of the (0002) peak intensity of V₂CT_x during discharge, and the (0002) peak also downshifted from 9.21° to 9.11°, which correponded to 0.1 Å increase in the d-spacing. Moreover, HRTEM images indicated that the interlayer spacing of V₂CT_r is increased by 0.2 Å after discharge. The XPS spectra show a reversible change of the vanadium oxidation state between V⁴⁺ and V³⁺. Clearly these active V sites are on the surface of V_2CT_x enabled by the functional groups. The V_2CT_x MXene layers were further exfoliated using tetrabutylammonium hydroxide to increase the interlayer spacing by 5.73 Å. The exfoliated V_2CT_x has a high specific capacity of 392 mA h g⁻¹ in the first cycle at a current density of 100 mA g^{-1} , which should be attributed to the enriched active surface sites containing V with a high oxidation state. In principle, MXene materials should not be categorized as Al3+ intercalation cathode materials since their electrochemical activity is provided by the surface functional groups resulting from the etching process.

2.5 Prussian blue analogues

Prussian blue analogues (PBAs) are three-dimensional open framework structures with large interstitial sites, 73-75 which are capable of accommodating the intercalation of guest ions such as Li⁺, Na⁺, K⁺, Mg²⁺, Zn²⁺, and Al³⁺. ⁷⁶⁻⁸³ PBAs were mainly studied as Al3+ intercalation type electrodes in RABs based on aqueous electrolytes similar to the ones used in the studies of transition metal oxide cathodes (AlCl₃, Al(OTf)₃, Al₂(SO₄)₃, or Al(NO₃)₃ in water). Reversible discharge and charge behaviors were demonstrated, and the redox of the transition metal centers during discharge and charge was confirmed in these studies. However, evidence of Al intercalation was lacking. Similar to transition metal oxide cathodes, PBA compounds are also known for highly reversible proton intercalation in acidic electrolytes.84 Furthermore, research shows that the same PBA compound had drastically different behavior toward Al intercalation in aqueous electrolyte versus organic electrolyte: Liu et al. reported that copper hexacyanoferrate (CuHCF) nanoparticles in aqueous Al₂(SO₄)₃ electrolyte could exhibit reversible intercalation of Al3+ in the voltage range of 0.2 to 1.2 V versus a saturated calomel reference electrode with a specific capacity of 58.9 mA h g⁻¹ at 50 mA g⁻¹. On the other hand, Menke and coworkers demonstrated that CuHCF had a very low reversible capacity (between 5 and 14 mA h g⁻¹) in Al(OTf)₃ electrolyte in diglyme within an electrochemical window between 0.1 and 0.7 V versus Al.85 These discrepancies suggest that the mechanism of PBAs in aqueous RABs requires further investigation.

3. Conversion mechanism cathode materials

Unlike intercalation-type cathode materials that require feasible crystal structures, conversion-type cathodes are more straightforward, at least theoretically. Most of the reported cathode materials for RABs to date are conversion-type. For example, the transition metals in CuO, 86 Co₃O₄, 87 FeS₂, 88 NiS, 89 and Ni₃S₂ 90 electrodes can be reduced to a low valence state after discharge and generating Al₂O₃ or Al₂S₃. The transition metals in Ni₂P, 91 Co₂P, 92 Co₃(PO₄)₂93 and CoSe₂94 cathodes will be reduced to the zero-valent state during conversion.

3.1 Transition metal oxides

CuO porous microspheres from hydrothermal methods were reported as cathode materials for RABs.86 A reduction peak at 0.6 V and an oxidation peak of 0.8 V versus Al were detected in

the CV curves. However, the charge-discharge curves demonstrate one additional discharge plateau at 0.2 V and one additional charge plateau at 2.0 V, which were not clearly explained. But one can speculate that the reductive decomposition of the chloroaluminate ionic liquid electrolyte could be the reason for the low discharge plateau, and chlorine generation could be the reaction for the high charging plateau.²⁹ Monovalent Cu⁺ was detected in the XPS spectra, confirming the reduction of Cu²⁺. The authors claimed Cu2O and Al2O3 as the products from the complete discharge to 0.1 V, however, the XRD pattern of the discharge products was inconclusive. Jiao and coworkers reported a metal organic framework (MOF)-derived Co₃O₄ polyhedral cathode for RABs.87 The CV curves demonstrated two reduction peaks at 0.6 V and 0.4 V and one oxidation peak at 0.97 V versus Al. The XPS Co 2p spectra indicated the existence of metallic Co in fully discharged Co₃O₄ (at 0.1 V). The XPS Al 2p spectra after discharge displayed the enhancement of the Al peak, which was attributed to the Al₂O₃ product.

3.2 Transition metal sulfides and selenides

Most of the conversion-type cathode materials for RABs are transition metal sulfides and selenides. Mori et al. studied FeS₂ as a cathode material for RABs at 55 °C.88 The ex situ XRD detected the FeS diffraction peak after the discharge of FeS2, and the FeS peak disappeared after full charging. The S K-edge XANES spectra indicate that the peak at 2472 eV decreases during discharging, and the S 1s is gradually transformed to the S 3p bond, which is reversed during the charging process

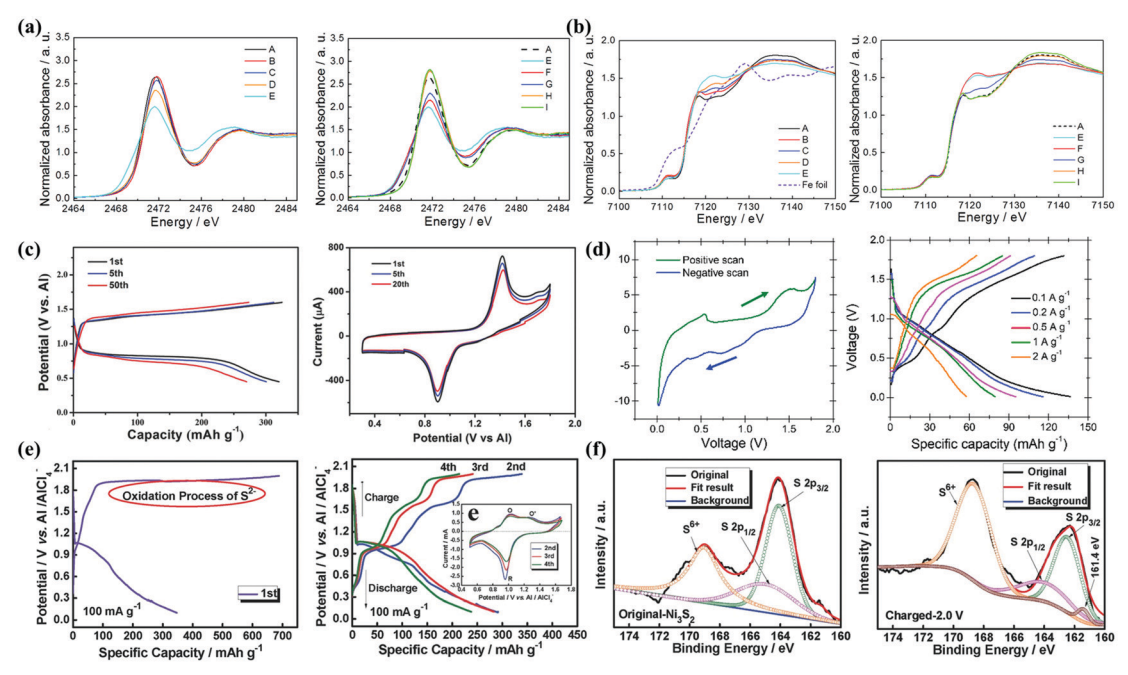


Fig. 5 (a) S K-edge and (b) Fe K-edge XANES spectra of FeS₂ during discharge and charge at 55 °C; potential decreases from A (OCP 1.2 V) to E (0.01 V) during discharge, and increases from E to I (1.8 V) during charge. Reproduced with permission from ref. 88. Copyright (2016) Elsevier. (c) The dischargecharge curves of binder-free Co₉S₈@CNT-CNF at 100 mA g⁻¹ and CV curves at 0.5 mV s⁻¹. Reproduced with permission from ref. 95. Copyright (2017) WILEY. (d) CV curves of Co₉S₈ versus Al at a scan rate of 0.25 mV s⁻¹ and the discharge-charge curves at different current density. Reproduced with permission from ref. 96. Copyright (2019) Elsevier. (e) The discharge-charge curves of Ni₃S₂/graphene at a current density of 100 mA g⁻¹; (f) S 2p XPS spectra of Ni₃S₂ in the pristine state and after full charge. Reproduced with permission from ref. 90. Copyright (2016) WILEY.

(Fig. 5a). On the other hand, no shift is detected in the absorption edge of the Fe K-edge XANES spectra (at 7115 eV), indicating that the oxidation state of Fe is unchanged during discharge and charge (Fig. 5b). The isosbestic point at 7130 eV reveals the coexistence of the two iron compounds in the electrode with no presence of metallic iron, which is consistent with the ex situ XRD results. Furthermore, S and Al K-edge XANES proved the existence of amorphous Al₂S₃. Therefore, the conversion reaction mechanism is described as the redox reaction between S₂²⁻ and S²⁻ (i.e., FeS₂ and FeS) accompanied by the formation of amorphous Al₂S₃. It is worth noting that the authors found that FeS2 and Al2S3 were readily soluble in the chloroaluminate ionic liquid, which would certainly complicate the discharge-charge process.

Zhuang and coworkers reported a binder-free cobalt disulfide and carbon nanofiber composite (CoS₂@CNFs) cathode.⁹⁷ The XPS analysis indicated that the oxidation state of Co in the pristine CoS_2 is Co^{2+} , and the anion is S_2^{2-} disulfide. Interestingly, Co³⁺ was detected from the XPS spectra after discharge, indicating that $S_2^{\,2-}$ must be reduced during discharge. Based on the XRD pattern of the discharge product, the authors proposed AlCo₂S₄ as the discharge product, although unknown peaks were detected. Co₉S₈ is another cobalt sulfide material being investigated for RABs. Wang and coworker reported a binder-free Co₉S₈@CNT-CNF cathode with an ultra-long cycle performance.95 The charge plateau (1.30 V) and discharge plateau (0.95 V) of the charge-discharge curve are consistent with the anodic and cathodic peaks of the CV curve (Fig. 5c). The XPS spectra indicates the reversible redox of Co during discharge and charge. Hu et al. also demonstrated a twodimensional porous Co₉S₈ nanosheet cathode with a capacity of 120 mA h g⁻¹ after 250 cycles at 0.2 A g⁻¹. However, the electrochemical characteristics of the porous Co₉S₈ nanosheets are quite different from the Co₉S₈@CNT-CNF reported by Wang as illustrated from the CV scan and the discharge-charge curves in Fig. 5d. It is clear that the detailed mechanism of Co₉S₈ needs further clarification.

Wang et al. reported two types of nickel sulfides including Ni₃S₂/graphene composite⁹⁰ and NiS nanobelts⁸⁹ as the cathode materials for RABs. It is worth noting that the Ni₃S₂ cathode is charged first before discharging due to the low valent states of Ni $(\mathrm{Ni}^0$ and Ni^{2^+} coexist in $\mathrm{Ni}_3\mathrm{S}_2)$. Peculiarly, the first charging curve is a long voltage plateau at 2.0 V versus Al with a capacity two times higher than that of the discharge (Fig. 5e). The XPS Ni 2p spectrum of the charged Ni₃S₂ indicates the disappearance of metallic Ni (characteristic peak at 852.8 eV), confirming the oxidization of Ni⁰ in Ni₃S₂. As displayed in Fig. 5f, the S 2p spectrum after charging shows a new peak at 161.4 eV, which is attributed by the authors to a small amount of NiS. 98 Furthermore, the S 2p spectrum after charging indicates reduced population of S²⁻ anions and increased population of oxidized sulfur species. Therefore, the authors speculate that the long charging plateaus are due to the oxidation of S²⁻. The high plateau at 2.0 V also appears in the subsequent cycles, but with lower capacity. It is necessary to point out that the deconvolution of the XPS S 2p spectra in this work has some flaws: S $2p_{1/2}$ and S $2p_{3/2}$ peaks must appear in pair

with a fixed peak separation of 1.16 eV and intensity ratio of 0.51. The S 2p spectra shown in Fig. 5f are not rigorously deconvoluted, therefore the interpretation may be questionable. Nevertheless, ex situ XRD showed that the charging products contain Al₂S₃, NiCl₂, and NiS. NiS can be rationalized as the oxidation product of Ni₃S₂ (due to the oxidation of Ni⁰), however the origin of Al₂S₃ and NiCl2 is not explained. The TEM images and selected area electron diffraction (SAED) after the reaction showed the transfer of Ni₃S₂ to amorphous structure, which is consistent with the conversion-type mechanism and may be the cause of the decrease in capacity. The same group subsequently studied hexagonal NiS nanobelt cathodes, 89 which is supposed to be the charging product of Ni₃S₂ according to their previous study. Indeed, the demonstrated electrochemical properties of NiS are consistent with Ni₃S₂.

Based on the experimental data presented in the two studies above, there is an alternative explanation for the redox mechanism of Ni₃S₂ in the chloroaluminate ionic liquid electrolyte: during the charge of Ni₃S₂, the metallic Ni is oxidized to NiCl₂ represented by the high changing plateau, which can explain the origin of the NiCl₂ identified by XRD. NiCl₂ is electrochemically active in the chloroaluminate ionic liquid. Shi et al. demonstrated that metallic Ni foil can function as an active cathode in Al-Ni cells by forming NiCl₂ through charge-first cycling.²⁹

Wang et al. prepared a hierarchical CuS microsphere cathode for RABs with a reversible capacity of 90 mA h g⁻¹ at a current density of 20 mA $\rm g^{-1}$ after 100 cycles. 99 The XPS Cu 2p spectra demonstrate a reversible redox reaction between Cu²⁺ and Cu⁺ during discharging and charging. The XRD pattern of the discharged electrode indicates the existence of Cu₂S and Al₂S₃. The Raman peak of CuS at 473.56 cm⁻¹ also shifted to 470.57 cm⁻¹ after discharge, indicating the conversion of CuS to Cu₂S.¹⁰⁰

Transition metal selenides were also investigated as the cathode materials for RABs including the cobalt selenidecarbon composite (CoSe@C) derived from MOF ZIF-67, 24 cobalt diselenide-carbon composite in a reduced graphene oxide framework (CoSe₂-C@rGO), 94 and 3D ordered microporous (3DOM) CoSe₂@C also derived from MOF ZIF-67.¹⁰¹ Despite their different chemical compositions and structures, these three cobalt selenides demonstrated very similar electrochemical properties, evidenced by the same feature in the chargedischarge curve and CV scan: a distinct charging plateau (or oxidization peak in CV) at approximately 2.0 V versus Al. It is also worth noting that none of the studies clearly stated whether charging (oxidation scan) or discharging (reduction scan) was applied first in their cycling (CV) experiments, which is critical to understand the reaction mechanism. All three studies provided XPS Co 2p spectra after cycling, but they are not fully self-consistent: the Co 2p spectrum of CoSe indicated that the valent state of Co (Co²⁺) does not change throughout charge and discharge; while the Co 2p spectra of CoSe₂ indicated the existence of metallic Co after both discharge and charge, which can be confusing, particularly without knowing if CoSe₂ was charged first or discharged first. However, what is consistent in all three studies is the XPS Se 3d spectra, which all indicate that Se anions (Se²⁻ in CoSe and Se₂²⁻ in CoSe₂) were oxidized in

the charging process. The authors of the CoSe study speculated that the Se²⁻ anion was oxidized to the positive valence state of Se^{x+} (x may be 4 or 6) after charging. Instead, the authors of the 3DOM CoSe₂@C study believed that Se₂²⁻ is oxidized to elemental Se. Nevertheless, it seems that redox of Se may be the main contributor to the demonstrated capacity of these cobalt selenides. Elemental Se has been demonstrated to be electrochemically active toward Al in the chloroaluminate ionic liquid electrolyte, 102-105 therefore the working mechanism of cobalt selenides (particularly the role of Co) needs further clarification. It is also worth mentioning that the high potential charge plateau and the corresponding discharge plateau resembles the charge and discharge plateaus from the AlCl₄ intercalation in graphitic carbon, thus whether Cl⁻ is involved in the charge and discharge reactions of the cobalt selenides also needs further investigation.

3.3 Phosphides and phosphate

Tu et al. studied nickel phosphide-reduced graphene oxide (Ni₂P-rGO) nanosheets as the cathode in RABs. 91 The distinct potential plateau of the initial charging curve at 1.9 V was attributed to potential side reactions of the electrolyte. Three oxidation peaks (0.99 V, 1.35 V and 1.80 V) and two reduction peaks (0.53 V and 0.85 V) were detected in the CV scans, corresponding to the multi-step platform of charge and discharge curves. Ex situ XRD showed that the peak intensity of the Ni₂P was significantly lowered after discharge, and the crystallinity increased after charging. The XPS spectra after discharge indicated the peaks of metallic Ni (853.4 eV and 871.0 eV) and Ni²⁺ (856.2 eV and 874.4 eV). TEM image and SAED after discharge confirmed the formation of metallic Ni. The change in the valence state of P indicates that Ni²⁺ is partially irreversibly reduced to metallic Ni after discharge.

Lu et al. synthesized a Co-P compound supported on carbon cloth (Co-P/CC) as the cathode for RABs. 92 XRD analysis confirmed the Co-P/CC is composed of polycrystal Co₂P and mellitic Co nanoparticles. The Co-P/CC composite demonstrated higher reversible capacity and lower voltage hysteresis compared to the commercial crystalline Co₂P. The oxidation peak at 1.0 V and two reduction peaks of 0.55 and 0.7 V in the CV curves corresponded to the potential plateau of the charge and discharge curve, while the 1.9 V charge plateau (not detected in CV) might be attributed to side reactions of the electrolyte. The XPS spectra showed the binding energy of metallic Co increased slightly (781.2 and 797.0 eV) when discharged to 0.01 V, and the peaks of Co²⁺ (781.2 and 797.0 eV) were detected after charging to 2.4 V, and the peaks of metallic Co disappeared. There was no change in the P 2p spectra, which confirmed that Co²⁺ in the Co-P/CC electrode is partially reduced to metallic Co during discharge. In addition, the peak intensity of Al 2p after discharge is increased, and the peak intensity of Cl 2p remained the same before and after discharge. Thus, the Co-P/CC cathode underwent a conversion reaction between Al3+ and Co2P during discharge to generate Al_mCo_nP and a small amount of metallic Co, which in turn was oxidized to Co₂P during the charging process. However, the contribution of the metallic Co in the pristine Co-P/CC composite to the charge/discharge capacity is unknown.

Yin and coworkers reported a cobalt phosphate-carbon composite $(Co_3(PO_4)_2@C)$ as the cathode of RABs.⁹³ This composite was obtained by carbonization of ZIF-67@RF (resorcinol formaldehyde) followed by NH4H2PO4 etching and heat treatment. The in situ XRD indicated a new peak (24.7°) was generated during discharge from 1.8 V to 0.9 V, and the peak intensity of the (210) plane at 25.9° was reduced. The appearance of the new peak during discharge is attributed to the generation of $Al_mCo_n(PO_4)_2$, and the in situ XRD patterns confirm the reappearance of the characteristic peaks of Co₃(PO₄)₂ after charging. Moreover, the XPS spectra showed the peak intensity of Co 2p_{1/2} and Co 2p_{3/2} is reduced after discharge, and the signal of Co⁰ was detected at 0.5 V. The Co 2p spectrum returned to the argininal state after charging to 2.3 V.

3.4 Sulfur and selenium electrodes

The conversion reaction between Al³⁺ and sulfur has a relatively high theoretical potential (about 1.3 V versus Al) and an excellent theoretical specific capacity of 1675 mA h g⁻¹. ^{106,107} Therefore, sulfur has been regarded as the most promising cathode for RABs. The main challenges of the sulfur cathode in RABs include the high hysteresis of the discharge and charge voltage and the slow reaction kinetics. 108 Transition metals have been demonstrated as effective catalysts for Li-S electrochemical reactions. 109,110 Similarly, MOF-derived Cu-containing hosts were used as the sulfur host in Al-S batteries to improve the kinetics of sulfur species conversion. Guo et al. reported a S@HKUST-1-C composite cathode decorated with Cu nanoparticles (Fig. 6a). 111 The first discharge capacity reached 1200 mA h g⁻¹, and the capacity retention was 460 mA h g⁻¹ after 500 cycles under 1 A g^{-1} (Fig. 6b). The same group subsequently reported a ZIF-67 derived Co-containing carbon host material for Al-S batteries. 112 The demonstrated capacity retention of the S@Co/C electrode was 500 mA h g-1 after 200 cycles at 1 A g⁻¹. The CV curve indicated a lower dischargecharge hysteresis of S@Co/C compared to S@C without the Co, confirming the catalytic effect of the Co content (Fig. 6c and d). In addition to the conventional redox reaction between elemental sulfur and sulfide anion (S²⁻), a unique sulfur redox mechanism in which sulfur can be reversibly oxidized to the positive valent state in chloroaluminate ionic liquids was recently demonstrated by Qiao and coworkers. 113 This work demonstrated redox of sulfur in two distinct windows: redox between S⁰ and S²⁻ with Al₂S₃ as the reduction product and the redox between S⁰ and S⁴⁺ with AlSCl₇ as the oxidation product (Fig. 6e and f). In situ near-edge X-ray absorption fine structure spectroscopy confirmed SCl₃⁺ as the intermediate product of the electrochemical oxidation of sulfur. This finding lays the groundwork for high-voltage rechargeable Al-S batteries.

The electrochemical properties of Se and S are considered similar, however Se has a great advantage of being significantly more conductive (1 \times 10⁻³ S m⁻¹ of Se *versus* 0.5 \times 10⁻²⁷ S m⁻¹ of S). It is interesting that similar to sulfur, Se can also be reversibly oxidized in chloroaluminate ionic liquid electrolytes. Huang et al. constructed a Se/CMK-3 composite as the cathode for Al-Se

Materials Chemistry Frontiers

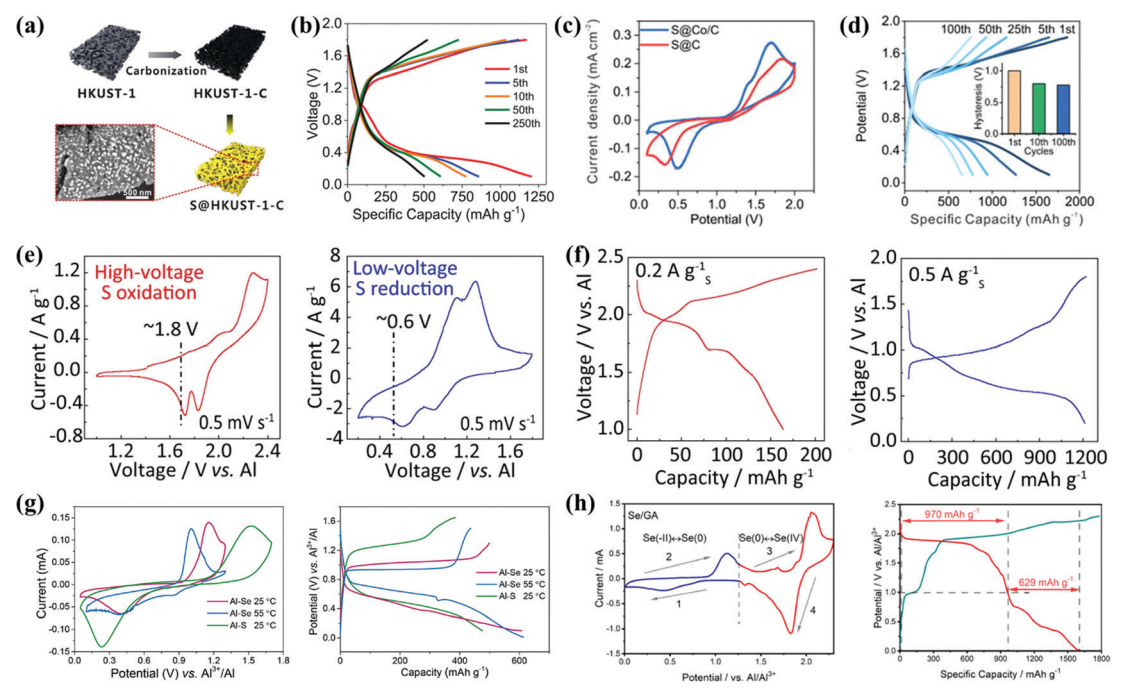


Fig. 6 (a) Schematic diagram of the synthesis of S@HKUST-1-C; (b) discharge-charge curves of S@HKUST-1-C at a current density of 1 A g^{-1} . Reproduced with permission from ref. 111. Copyright (2018) WILEY. (c) CV curves of S@Co/C and S@C cathodes at 0.2 mV s⁻¹; (d) discharge-charge curves of S@Co/C at 1 A g⁻¹; the inset shows the discharge-charge hysteresis at different cycles. Reproduced with permission from ref. 112. Copyright (2020) WILEY. (e) CV curves and (f) discharge-charge potential profiles of the S/CNT cathode in electrochemical widows with different cutoff potentials. Reproduced with permission from ref. 113. Copyright (2021) The Author(s). (g) CV scans and the discharge-charge curves of S@CMK-3 and Se@CMK-3 cathodes at 25 °C and 55 °C. Reproduced with permission from ref. 104. Copyright (2019) Elsevier. (h) CV curves of Se/GA at a scan rate of 0.2 mV s⁻¹ and discharge-charge curves at 100 mA $\rm g^{-1}$, the capacity is contributed from the two-stage reaction between $\rm Se^{2-}$ and $\rm Se^{4+}$. Reproduced with permission from ref. 105. Copyright (2021) Elsevier.

batteries, 102 in which it was charged first to 2.3 V versus Al in the charge-discharge tests. The charge product was identified as selenium chloride (Se₂Cl₂). Therefore, the electrochemical mechanism is the redox reaction between Se⁰ and Se₂²⁺. A reversible capacity of 178 mA h $\rm g^{-1}$ at 100 mA $\rm g^{-1}$ was demonstrated for 50 cycles with a nominal discharge voltage of 1.8 V versus Al. Interestingly, Liu et al. studied the redox reaction of the same Se@CMK-3 cathode using a discharge-first protocol with a cut-off charging voltage at 1.5 V versus Al (Fig. 6g). 104 It was found that the reversible redox reaction is between Se⁰ and Se²⁻ anions with Al₂Se₃ as the discharge product. Li et al. reported a Se-carbon nanotube (Se@CT) composite cathode. 103 The reversible Se oxidation was also demonstrated in this study with a capacity of 163 mA h g⁻¹ at 500 mA g⁻¹ for 200 cycles. However, the authors argued a high valence state of Se such as Se4+ and Se2+ in addition to Se22+ could be the products of charging, which could lead to higher capacity. It is clear that Se is capable of a wide range of redox reactions between positive and negative valence states enabled by the chloroaluminate ionic liquid electrolyte. Yan and coworkers demonstrated a selenium/graphene aerogel composite (Se/GA) cathode in AlCl₃/triethylamine hydrochloride ionic liquid electrolyte. 105 The authors proved that different electrochemical reactions occur in the two voltage ranges of 0.01 to 1.5 V and 1.0 to 2.3 V versus Al. The 6-electron transfer mechanism of Se (Se²⁻ \leftrightarrow Se⁰ \leftrightarrow Se⁴⁺) was demonstrated with a theoretical capacity of 2036 mA h g⁻¹.

In fact, the Se/GA cathode delivered a specific capacity of 1599 mA h g⁻¹ (Se⁰ \leftrightarrow Se⁴⁺ contributing \sim 970 mA h g⁻¹ and $Se^{2-} \leftrightarrow Se^0$ contributing ~629 mA h g⁻¹) at a current density of 100 mA g⁻¹, reaching a utilization of 78.5% (Fig. 6h). It is worth noting that the high redox potential (approximately 1.85 and 2.06 V versus Al) between Se and the oxidized Se species are very similar to that of some transition metal selenide cathodes for RABs. 24,94,101,114,115 The similarity implies that these transition metal selenides may have Se_x^{2-} anions as the active species contributing to the demonstrated reversible capacity.

3.5 Organic cathode materials

Organic redox materials have been extensively studied as cathode materials for rechargeable Li-ion batteries. RABs can also potentially benefit from the organic cathodes due to their robust redox mechanisms and high redox potential relative to Al compared to the inorganic materials. Conducting polymers, specifically polypyrrole and polythiophene, were studied by Hudak as the cathode materials for RABs. 116 It was found that both polymers can be reversibly oxidized and reduced in the chloroaluminate ionic liquid electrolytes with chloroaluminate anions functioning as the dopants for the conducting polymers. Stable specific capacity between 30 to 100 mA h g⁻¹ was demonstrated. More recent organic cathodes for RABs are based on the reversible reduction of the quinones and the coordination of chloroaluminate cations, including monovalent

AlCl₂⁺ and divalent AlCl²⁺, to the guinones after reduction. Stoddart and coworkers studied a phenanthrenequinone (PQ) based cathode in a Lewis acidic chloroaluminate ionic liquid electrolyte, and confirmed the reversible reduction of the quinone and the coordination of monovalent AlCl₂⁺ in PQ. This organic cathode demonstrated superior capacity retention and rate capability compared to typical inorganic cathodes: retaining 53 mA h g⁻¹ after 5000 cycles at 2 A g⁻¹. Lu and coworkers studied a polyimide/MOF composite cathode with a capacity of 73 mA h $\rm g^{-1}$ after 2800 cycles under 1 A $\rm g^{-1}$. 118 A similar reaction mechanism involving monovalent AlCl₂⁺ was proposed. Dominko and colleagues revealed the redox reaction of anthraquinone (AO) in the chloroaluminate ionic liquid, and they further developed an anthraquinone-based poly(antraquinonyl sulfide) (PAQS) cathode for RABs. 119 The PAOS cathode demonstrated an initial discharge capacity of 190 mA h g⁻¹ at 0.5C and a 60% retention after 500 cycles. The authors proposed that the electrochemical mechanism was the reduction of the quinone accompanied with the coordination of the divalent AlCl2+. Choi and coworkers reported a tetradiketone (TDK) macrocyclic molecule, which can reversibly react with AlCl²⁺ to achieve a high initial capacity of 350 mA h g⁻¹ and excellent stability of 8000 cycles. ¹²⁰ Compared with PQ that reacts with the monovalent $AlCl_2^+$, the authors proposed that TDK prefers coordination with divalent AlCl²⁺ due to its low stabilization after reduction from the lower ratio of benzene ring to carbonyl. The DFT calculation of binding energy, calculated IR vibration peaks of TDK, and the achieved specific capacity all supported the hypothesis that TDK coordinated with divalent AlCl2+.

4. Conclusion and outlook

In summary, a number of challenges exist in the current field of Al³⁺ intercalation and conversion-type cathode materials for RABs. For intercalation-type cathodes, Chevrel Phase Mo₆S₈ is the only material that has been proven to follow this kind of mechanism with unambiguous evidence. Other Chevrel phase materials can also be expected to host Al via intercalation, however, with the low specific capacity (due to high molecular mass) and low intercalation-extraction potential versus Al, their practical value is questionable. Although many intercalationtype materials for monovalent cations have been claimed to be capable of hosting Al3+ via intercalation too, unambiguous experimental evidence such as crystallographic data is lacking in current studies. XPS has become a conventional technique to characterize the claimed intercalation-type cathode, however, XPS can only reveal the valence state of surface elements and cannot provide crystal structural information. It is critical for studies on Al3+ intercalation materials to show unambiguous crystallographic evidence. Furthermore, the desolvation of chloroaluminate anions during Al3+ intercalation must be understood.

We believe most of the reported RAB cathode materials are conversion-type based on our analysis of literature. The conversion mechanism may be straightforward in Li-ion batteries, but it can be

complex in RABs due to the involvement of the chloroaluminate ionic liquid electrolytes. The first question that has not been clearly answered is the chemical compatibility of the transition metal oxides, chalcogenides, and phosphides with the ionic liquids. A number of studies clearly demonstrate that some metal oxides and sulfides either dissolve in or react with the chloroaluminate ionic liquids. It is important for researchers to check the chemical compatibility of the cathode materials prior to the study of their electrochemical properties. Some studies on conversion-type cathodes indicated the existence of a metallic transition metal such as Ni or Co, thus it must be realized that these metals can be either corroded or electrochemically active in the ionic liquids. For instance, Ni, Ti, and Cu can be oxidized to form their chloride salts in the charging process in the chloroaluminate ionic liquids, and these chloride salts can be cycled in the charge-discharge tests demonstrating battery-like behavior. The true electrochemical reactions during the cycling of the RABs may not be the intended ones. A good example of this statement is the RABs based aqueous electrolytes. Another question about conversion-type cathodes is the role of chalcogenide anions, particularly selenides. A number of studies suggest that selenide anions can be oxidized (charged) to positive valence states, which would significantly improve the specific capacity of these materials.

Sulfur and selenium are more promising conversion-type cathode materials compared to the ones based on transition metals due to their clear advantage in capacity. The cycling performance of Al-S batteries has been demonstrated, but the reaction mechanism involving the intermediate products is not fully understood. An analogous reaction mechanism to that in Li-S batteries cannot be assumed in Al-S batteries due to the chloroaluminate ionic liquid electrolytes. Some interesting electrochemical properties of Al-S and Al-Se batteries have been demonstrated, specifically in the wide redox range of S and Se from negative to positive valence states, which can provide an additional boost to their specific capacity. The current studies suggest that the oxidation of S and Se to the positive valence state is enabled by the chloroaluminate anions (i.e., forming AlSCl7 and Se2Cl2) featured by a high charging plateau around 2 V versus Al. However, this potential is very close to the chlorine generation potential, particularly on cathodes using carbon materials with a high surface area, which can lower the overpotential of chlorine generation. Therefore, it may be possible that the charging products of S or Se in a high oxidation state such as Se₂Cl₂ are not directly from electrochemical oxidation of Se⁰, instead, they may be a result of the chemical reaction between Se and the chlorine generated during the charging process at high potential. The performance degradation of Al-S and Al-Se batteries also originates from the shuttle effect, dissolution of intermediate products in the chloroaluminate ionic liquid electrolytes. 113,121 How to suppress the shuttle effect is the key to improving the cycle stability of Al-S and Al-Se RABs.

All current studies indicate that the chloroaluminate ionic liquid electrolyte is a universal problem for RABs. Although it is not the focus point of this critical review, it is clear that chloroaluminate ionic liquids are not feasible electrolytes for

practical RABs. They are expensive, corrosive, prone to oxidation (chlorine generation), and actively react with many cathode materials. Research and development of new Al electrolytes is crucial for RAB technologies.

Conflicts of interest

The authors declare no conflict of interest.

Acknowledgements

This work was supported in part by the National Natural Science Foundation of China (No. 21875223). J. G. acknowledges the support from the U.S. National Science Foundation through grant CBET-1751929.

References

- 1 Y. Liang, H. Dong, D. Aurbach and Y. Yao, Current status and future directions of multivalent metal-ion batteries, Nat. Energy, 2020, 5(9), 646-656.
- 2 G. A. Elia, K. Marquardt, K. Hoeppner, S. Fantini, R. Lin, E. Knipping, W. Peters, J. F. Drillet, S. Passerini and R. Hahn, An Overview and Future Perspectives of Aluminum Batteries, Adv. Mater., 2016, 28(35), 7564-7579.
- 3 E. Faegh, B. Ng, D. Hayman and W. E. Mustain, Practical assessment of the performance of aluminium battery technologies, Nat. Energy, 2020, 6(1), 21-29.
- 4 F. Wu, H. Yang, Y. Bai and C. Wu, Paving the Path toward Reliable Cathode Materials for Aluminum-Ion Batteries, Adv. Mater., 2019, 31(16), e1806510.
- 5 F. Ambroz, T. J. Macdonald and T. Nann, Trends in Aluminium-Based Intercalation Batteries, Adv. Energy Mater., 2017, 7(15), 1602093.
- 6 M. C. Lin, M. Gong, B. Lu, Y. Wu, D. Y. Wang, M. Guan, M. Angell, C. Chen, J. Yang, B. J. Hwang and H. Dai, An ultrafast rechargeable aluminium-ion battery, Nature, 2015, 520(7547), 324-328.
- 7 Z. Rong, R. Malik, P. Canepa, G. Sai Gautam, M. Liu, A. Jain, K. Persson and G. Ceder, Materials Design Rules for Multivalent Ion Mobility in Intercalation Structures, Chem. Mater., 2015, 27(17), 6016-6021.
- 8 W. Wang, B. Jiang, W. Xiong, H. Sun, Z. Lin, L. Hu, J. Tu, J. Hou, H. Zhu and S. Jiao, A new cathode material for super-valent battery based on aluminium ion intercalation and deintercalation, Sci. Rep., 2013, 3, 3383.
- 9 H. Wang, Y. Bai, S. Chen, X. Luo, C. Wu, F. Wu, J. Lu and K. Amine, Binder-free V₂O₅ cathode for greener rechargeable aluminum battery, ACS Appl. Mater. Interfaces, 2015, 7(1), 80-84.
- 10 S. Gu, H. Wang, C. Wu, Y. Bai, H. Li and F. Wu, Confirming reversible Al3+ storage mechanism through intercalation of Al3+ into V2O5 nanowires in a rechargeable aluminum battery, Energy Storage Mater., 2017, 6, 9-17.

- 11 J. Jiang, H. Li, J. Huang, K. Li, J. Zeng, Y. Yang, J. Li, Y. Wang, J. Wang and J. Zhao, Investigation of the Reversible Intercalation/Deintercalation of Al into the Novel Li₃VO₄@C Microsphere Composite Cathode Material for Aluminum-Ion Batteries, ACS Appl. Mater. Interfaces, 2017, 9(34), 28486-28494.
- 12 H. Wang, X. Bi, Y. Bai, C. Wu, S. Gu, S. Chen, F. Wu, K. Amine and J. Lu, Open-Structured V₂O₅·nH₂O Nanoflakes as Highly Reversible Cathode Material for Monovalent and Multivalent Intercalation Batteries, Adv. Energy Mater., 2017, 7(14), 1602720.
- 13 H. Lu, Y. Wan, T. Wang, R. Jin, P. Ding, R. Wang, Y. Wang, C. Teng, L. Li, X. Wang, D. Zhou and G. Xue, A high performance SnO₂/C nanocomposite cathode for aluminumion batteries, J. Mater. Chem. A, 2019, 7(12), 7213-7220.
- 14 L. Geng, G. Lv, X. Xing and J. Guo, Reversible Electrochemical Intercalation of Aluminum in Mo₆S₈, Chem. Mater., 2015, 27(14), 4926-4929.
- 15 L. Geng, J. P. Scheifers, C. Fu, J. Zhang, B. P. T. Fokwa and J. Guo, Titanium Sulfides as Intercalation-Type Cathode Materials for Rechargeable Aluminum Batteries, ACS Appl. Mater. Interfaces, 2017, 9(25), 21251-21257.
- 16 L. Geng, J. P. Scheifers, J. Zhang, K. N. Bozhilov, B. P. T. Fokwa and J. Guo, Crystal Structure Transformation in Chevrel Phase Mo₆S₈ Induced by Aluminum Intercalation, Chem. Mater., 2018, 30(23), 8420-8425.
- 17 H. Li, H. Yang, Z. Sun, Y. Shi, H.-M. Cheng and F. Li, A highly reversible Co₃S₄ microsphere cathode material for aluminum-ion batteries, Nano Energy, 2019, 56, 100-108.
- 18 Y. Tong, A. Gao, Q. Zhang, T. Gao, J. Yue, F. Meng, Y. Gong, S. Xi, Z. Lin, M. Mao, S. Peng, X. Wang, D. Xiao, D. Su, Y. Luo, H. Li, L. Chen, L. Suo and L. Gu, Cation-synergy stabilizing anion redox of Chevrel phase Mo₆S₈ in aluminum ion battery, Energy Storage Mater., 2021, 37, 87-93.
- 19 A. VahidMohammadi, A. Hadjikhani, S. Shahbazmohamadi and M. Beidaghi, Two-Dimensional Vanadium Carbide (MXene) as a High-Capacity Cathode Material for Rechargeable Aluminum Batteries, ACS Nano, 2017, 11(11), 11135-11144.
- 20 L. Wu, R. Sun, F. Xiong, C. Pei, K. Han, C. Peng, Y. Fan, W. Yang, Q. An and L. Mai, A rechargeable aluminum-ion battery based on a VS2 nanosheet cathode, Phys. Chem. Chem. Phys., 2018, 20(35), 22563-22568.
- 21 W. Yang, H. Lu, Y. Cao, B. Xu, Y. Deng and W. Cai, Flexible Free-Standing MoS₂/Carbon Nanofibers Composite Cathode for Rechargeable Aluminum-Ion Batteries, ACS Sustainable Chem. Eng., 2019, 7(5), 4861-4867.
- 22 Q. Zhou, D. Wang, Y. Lian, S. Hou, C. Ban, Z. Wang, J. Zhao and H. Zhang, Rechargeable aluminum-ion battery with sheet-like MoSe₂@C nanocomposites cathode, *Electrochim*. Acta, 2020, 354, 136677.
- 23 X. Feng, J. Li, Y. Ma, C. Yang, S. Zhang, J. Li and C. An, Construction of Interlayer-Expanded MoSe₂/Nitrogen-Doped Graphene Heterojunctions for Ultra-Long-Cycling Rechargeable Aluminum Storage. ACS Appl. Energy, Mater., 2021, 4(2), 1575-1582.

- 24 W. Xing, D. Du, T. Cai, X. Li, J. Zhou, Y. Chai, Q. Xue and Z. Yan, Carbon-encapsulated CoSe nanoparticles derived from metal-organic frameworks as advanced cathode material for Al-ion battery, J. Power Sources, 2018, 401,
- 25 N. Jayaprakash, S. K. Das and L. A. Archer, The rechargeable aluminum-ion battery, Chem. Commun., 2011, 47(47), 12610-12612.
- 26 L. D. Reed and E. Menke, The Roles of V₂O₅ and Stainless Steel in Rechargeable Al-Ion Batteries, J. Electrochem. Soc., 2013, **160**(6), A915–A917.
- 27 A. M. Diem, B. Fenk, J. Bill and Z. Burghard, Binder-Free V₂O₅ Cathode for High Energy Density Rechargeable Aluminum-Ion Batteries, Nanomaterials, 2020, 10(2), 247.
- 28 A. M. Diem, J. Bill and Z. Burghard, Creasing Highly Porous V₂O₅ Scaffolds for High Energy Density Aluminum-Ion Batteries, ACS Appl. Energy Mater., 2020, 3(4), 4033-4042.
- 29 J. Shi, J. Zhang and J. Guo, Avoiding Pitfalls in Rechargeable Aluminum Batteries Research, ACS Energy Lett., 2019, 4(9), 2124-2129.
- 30 X. Wen, Y. Liu, A. Jadhav, J. Zhang, D. Borchardt, J. Shi, B. M. Wong, B. Sanyal, R. J. Messinger and J. Guo, Materials Compatibility in Rechargeable Aluminum Batteries: Chemical and Electrochemical Properties between Vanadium Pentoxide and Chloroaluminate Ionic Liquids, Chem. Mater., 2019, 31(18), 7238-7247.
- 31 S. Liu, J. J. Hu, N. F. Yan, G. L. Pan, G. R. Li and X. P. Gao, Aluminum storage behavior of anatase TiO2 nanotube arrays in aqueous solution for aluminum ion batteries, Energy Environ. Sci., 2012, 5(12), 9743-9746.
- 32 Y. Liu, S. Sang, Q. Wu, Z. Lu, K. Liu and H. Liu, The electrochemical behavior of Cl⁻ assisted Al³⁺ insertion into titanium dioxide nanotube arrays in aqueous solution for aluminum ion batteries, Electrochim. Acta, 2014, 143, 340-346.
- 33 M. Kazazi, P. Abdollahi and M. Mirzaei-Moghadam, High surface area TiO2 nanospheres as a high-rate anode material for aqueous aluminium-ion batteries, Solid State Ionics, 2017, 300, 32-37.
- 34 C. Wu, S. Gu, Q. Zhang, Y. Bai, M. Li, Y. Yuan, H. Wang, X. Liu, Y. Yuan, N. Zhu, F. Wu, H. Li, L. Gu and J. Lu, Electrochemically activated spinel manganese oxide for rechargeable aqueous aluminum battery, Nat. Commun., 2019, 10(1), 73.
- 35 S. He, J. Wang, X. Zhang, J. Chen, Z. Wang, T. Yang, Z. Liu, Y. Liang, B. Wang, S. Liu, L. Zhang, J. Huang, J. Huang, L. A. O'Dell and H. Yu, A High-Energy Aqueous Aluminum-Manganese Battery, Adv. Funct. 29(45), 1905228.
- 36 Y. Cai, S. Kumar, R. Chua, V. Verma, D. Yuan, Z. Kou, H. Ren, H. Arora and M. Srinivasan, Bronze-type vanadium dioxide holey nanobelts as high performing cathode material for aqueous aluminium-ion batteries, J. Mater. Chem. A, 2020, 8(25), 12716-12722.
- 37 J. R. González, F. Nacimiento, M. Cabello, R. Alcántara, P. Lavela and J. L. Tirado, Reversible intercalation of

- aluminium into vanadium pentoxide xerogel for aqueous rechargeable batteries, RSC Adv., 2016, 6(67), 62157-62164.
- 38 H. Lahan and S. K. Das, Al³⁺ ion intercalation in MoO₃ for aqueous aluminum-ion battery, J. Power Sources, 2019, 413,
- 39 P. Wang, Z. Chen, H. Wang, Z. Ji, Y. Feng, J. Wang, J. Liu, M. Hu, J. Fei, W. Gan and Y. Huang, A high-performance flexible aqueous Al ion rechargeable battery with long cycle life, Energy Storage Mater., 2020, 25, 426-435.
- 40 B. Jin, S. Hejazi, H. Chu, G. Cha, M. Altomare, M. Yang and P. Schmuki, A long-term stable aqueous aluminum battery electrode based on one-dimensional molybdenumtantalum oxide nanotube arrays, Nanoscale, 2021, 13(12), 6087-6095.
- 41 O. Zhao, L. Liu, J. Yin, J. Zheng, D. Zhang, J. Chen and L. A. Archer, Proton Intercalation/De-Intercalation Dynamics in Vanadium Oxides for Aqueous Aluminum Electrochemical Cells, Angew. Chem., Int. Ed., 2020, 59(8), 3048-3052.
- 42 S. Fleischmann, Y. Sun, N. C. Osti, R. Wang, E. Mamontov, D.-E. Jiang and V. Augustyn, Interlayer separation in hydrogen titanates enables electrochemical proton intercalation, J. Mater. Chem. A, 2020, 8(1), 412-421.
- 43 H. Guo, D. Goonetilleke, N. Sharma, W. Ren, Z. Su, A. Rawal and C. Zhao, Two-Phase Electrochemical Proton Transport and Storage in α -MoO₃ for Proton Batteries, *Cell* Rep. Phys. Sci., 2020, 1(10), 100225.
- 44 C. Li, X. Han, F. Cheng, Y. Hu, C. Chen and J. Chen, Phase and composition controllable synthesis of cobalt manganese spinel nanoparticles towards efficient oxygen electrocatalysis, Nat. Commun., 2015, 6, 7345.
- 45 P. Canepa, S. H. Bo, G. Sai Gautam, B. Key, W. D. Richards, T. Shi, Y. Tian, Y. Wang, J. Li and G. Ceder, High magnesium mobility in ternary spinel chalcogenides, Nat. Commun., 2017, 8(1), 1759.
- 46 L. Yin, B. J. Kwon, Y. Choi, C. J. Bartel, M. Yang, C. Liao, B. Key, G. Ceder and S. H. Lapidus, Operando X-ray Diffraction Studies of the Mg-Ion Migration Mechanisms in Spinel Cathodes for Rechargeable Mg-Ion Batteries, J. Am. Chem. Soc., 2021, 143(28), 10649-10658.
- 47 J. Cai, Z. Wang, S. Wu, Y. Han and J. Li, A Machine Learning Shortcut for Screening the Spinel Structures of Mg/Zn Ion Battery Cathodes with a High Conductivity and Rapid Ion Kinetics, Energy Storage Mater., 2021, 42, 277-285.
- 48 S. Saha, G. Assat, M. T. Sougrati, D. Foix, H. Li, J. Vergnet, S. Turi, Y. Ha, W. Yang, J. Cabana, G. Rousse, A. M. Abakumov and J.-M. Tarascon, Exploring the bottlenecks of anionic redox in Li-rich layered sulfides, Nat. Energy, 2019, 4(11), 977-987.
- 49 Q. Yun, L. Li, Z. Hu, Q. Lu, B. Chen and H. Zhang, Layered Transition Metal Dichalcogenide-Based Nanomaterials for Electrochemical Energy Storage, Adv. Mater., 2020, 32(1), e1903826.
- 50 J. Chen, D. H. C. Chua and P. S. Lee, The Advances of Metal Sulfides and In Situ Characterization Methods beyond Li

- Ion Batteries: Sodium, Potassium, and Aluminum Ion Batteries, Small Methods, 2020, 4(1), 1900648.
- 51 Y. Li, J. Qian, M. Zhang, S. Wang, Z. Wang, M. Li, Y. Bai, Q. An, H. Xu, F. Wu, L. Mai and C. Wu, Co-Construction of Sulfur Vacancies and Heterojunctions in Tungsten Disulfide to Induce Fast Electronic/Ionic Diffusion Kinetics for Sodium-Ion Batteries, Adv. Mater., 2020, 32(47), e2005802.
- 52 M. M. Thackeray, Exploiting the Spinel Structure for Li-ion Battery Applications: A Tribute to John B. Goodenough, Adv. Energy Mater., 2021, 11(2), 2001117.
- 53 L. F. Wan, B. R. Perdue, C. A. Apblett and D. Prendergast, Mg Desolvation and Intercalation Mechanism at the Mo6S8 Chevrel Phase Surface, Chem. Mater., 2015, 27(17), 5932-5940.
- 54 J. M. Tarascon, F. J. Disalvo, D. W. Murphy, G. W. Hull, E. A. Rietman and J. V. Waszczak, Stoichiometry and physical properties of ternary molybdenum chalcogenides $M_xMo_6X_8$ (X = S, Se; M = Li, Sn, Pb), J. Solid State Chem., 1984, 54(2), 204-212.
- 55 D. Aurbach, Z. Lu, A. Schechter, Y. Gofer, H. Gizbar, R. Turgeman, Y. Cohen, M. Moshkovich and E. Levi, Prototype systems for rechargeable magnesium batteries, Nature, 2000, 407(6805), 724-727.
- 56 E. Lancry, E. Levi, Y. Gofer, M. Levi, G. Salitra and D. Aurbach, Leaching Chemistry and the Performance of the Mo6S8 Cathodes in Rechargeable Mg Batteries, Chem. Mater., 2004, 16(14), 2832-2838.
- 57 P. Saha, P. H. Jampani, M. K. Datta, D. Hong, C. U. Okoli, A. Manivannan and P. N. Kumta, Electrochemical Performance of Chemically and Solid State-Derived Chevrel Phase Mo_6T_8 (T = S, Se) Positive Electrodes for Sodium-Ion Batteries. The, J. Phys. Chem. C, 2015, 119(11), 5771-5782.
- 58 T. R. Juran and M. Smeu, Hybrid density functional theory modeling of Ca, Zn, and Al ion batteries using the Chevrel phase Mo₆S₈ cathode, Phys. Chem. Chem. Phys., 2017, **19**(31), 20684-20690.
- 59 B. Lee, H. R. Lee, T. Yim, J. H. Kim, J. G. Lee, K. Y. Chung, B. W. Cho and S. H. Oh, Investigation on the Structural Evolutions during the Insertion of Aluminum Ions into Mo₆S₈ Chevrel Phase, J. Electrochem. Soc., 2016, 163(6), A1070-A1076.
- 60 D. Aurbach, Y. Gofer, Z. Lu, A. Schechter, O. Chusid, H. Gizbar, Y. Cohen, V. Ashkenazi, M. Moshkovich, R. Turgeman and E. Levi, A short review on the comparison between Li battery systems and rechargeable magnesium battery technology, J. Power Sources, 2001, 97-98, 28-32.
- 61 M. D. Levi, H. Gizbar, E. Lancry, Y. Gofer, E. Levi and D. Aurbach, A comparative study of Mg²⁺ and Li⁺ ion insertions into the Mo₆S₈ Chevrel phase using electrochemical impedance spectroscopy, J. Electroanal. Chem., 2004, 569(2), 211-223.
- 62 D. Aurbach, G. S. Suresh, E. Levi, A. Mitelman, O. Mizrahi, O. Chusid and M. Brunelli, Progress in Rechargeable Magnesium Battery Technology, Adv. Mater., 2007, 19(23), 4260-4267.

- 63 S. H. Choi, J. S. Kim, S. G. Woo, W. Cho, S. Y. Choi, J. Choi, K. T. Lee, M. S. Park and Y. J. Kim, Role of Cu in Mo₆S₈ and Cu mixture cathodes for magnesium ion batteries, ACS Appl. Mater. Interfaces, 2015, 7(12), 7016-7024.
- 64 H. Chu, J. Pan, S. Bai, Y. Ma, Y. Feng, Y. Wen, Y. Yang, R. Luo and A. Chen, Carbon coated chevrel phase of Mo₆S₈ as anode material for improving electrochemical properties of aqueous lithium-ion batteries, Electrochim. Acta, 2017, 258, 236-240.
- 65 M. Mao, Z. Lin, Y. Tong, J. Yue, C. Zhao, J. Lu, Q. Zhang, L. Gu, L. Suo, Y. S. Hu, H. Li, X. Huang and L. Chen, Iodine Vapor Transport-Triggered Preferential Growth of Chevrel Mo₆S₈ Nanosheets for Advanced Multivalent Batteries, ACS Nano, 2020, 14(1), 1102-1110.
- 66 W. Xue, Z. Shi, L. Suo, C. Wang, Z. Wang, H. Wang, K. P. So, A. Maurano, D. Yu, Y. Chen, L. Qie, Z. Zhu, G. Xu, J. Kong and J. Li, Intercalation-conversion hybrid cathodes enabling Li-S full-cell architectures with jointly superior gravimetric and volumetric energy densities, Nat. Energy, 2019, 4(5), 374-382.
- 67 M. Li, T. Liu, Z. Shi, W. Xue, Y. S. Hu, H. Li, X. Huang, J. Li, L. Suo and L. Chen, Dense All-Electrochem-Active Electrodes for All-Solid-State Lithium Batteries, Adv. Mater., 2021, 33(26), e2008723.
- 68 A. L. Jadhav, J. H. Xu and R. J. Messinger, Quantitative Molecular-Level Understanding of Electrochemical Aluminum-Ion Intercalation into a Crystalline Battery Electrode, ACS Energy Lett., 2020, 5(9), 2842-2848.
- 69 M. Naguib, M. Kurtoglu, V. Presser, J. Lu, J. Niu, M. Heon, L. Hultman, Y. Gogotsi and M. W. Barsoum, Two-Dimensional Nanocrystals Produced by Exfoliation of Ti₃AlC₂, Adv. Mater., 2011, 23(37), 4248-4253.
- 70 M. Naguib, V. N. Mochalin, M. W. Barsoum and Y. Gogotsi, 25th Anniversary Article: MXenes: A New Family of Two-Dimensional Materials, *Adv. Mater.*, 2014, **26**(7), 992–1005.
- 71 Z. Ling, C. E. Ren, M.-Q. Zhao, J. Yang, J. M. Giammarco, J. Qiu, M. W. Barsoum and Y. Gogotsi, Flexible and conductive MXene films and nanocomposites with high capacitance, Proc. Natl. Acad. Sci. U. S. A., 2014, 111(47), 16676.
- 72 B. Anasori, M. R. Lukatskaya and Y. Gogotsi, 2D metal carbides and nitrides (MXenes) for energy storage, Nat. Sci. Mater., 2017, 2(2), 16098.
- 73 L. Zhang, L. Chen, X. Zhou and Z. Liu, Towards High-Voltage Aqueous Metal-Ion Batteries Beyond 1.5 V: The Zinc/Zinc Hexacyanoferrate System, Adv. Energy Mater., 2015, 5(2), 1400930.
- 74 K. Hurlbutt, S. Wheeler, I. Capone and M. Pasta, Prussian Blue Analogs as Battery Materials, Joule, 2018, 2(10), 1950-1960.
- 75 L. Jiang, Y. Lu, C. Zhao, L. Liu, J. Zhang, Q. Zhang, X. Shen, J. Zhao, X. Yu, H. Li, X. Huang, L. Chen and Y.-S. Hu, Building aqueous K-ion batteries for energy storage, Nat. Energy, 2019, 4(6), 495-503.
- 76 M. Pasta, R. Y. Wang, R. Ruffo, R. Qiao, H.-W. Lee, B. Shyam, M. Guo, Y. Wang, L. A. Wray, W. Yang, M. F. Toney and Y. Cui, Manganese-cobalt hexacyanoferrate

- cathodes for sodium-ion batteries, J. Mater. Chem. A, 2016, 4(11), 4211-4223.
- 77 Y. Mizuno, M. Okubo, E. Hosono, T. Kudo, H. Zhou and K. Oh-ishi, Suppressed Activation Energy for Interfacial Charge Transfer of a Prussian Blue Analog Thin Film Electrode with Hydrated Ions (Li⁺, Na⁺, and Mg²⁺), J. Phys. Chem. C, 2013, 117(21), 10877-10882.
- 78 C. D. Wessells, S. V. Peddada, R. A. Huggins and Y. Cui, Nickel hexacyanoferrate nanoparticle electrodes for aqueous sodium and potassium ion batteries, Nano Lett., 2011, **11**(12), 5421-5425.
- 79 M. S. Chae, J. W. Heo, H. H. Kwak, H. Lee and S.-T. Hong, Organic electrolyte-based rechargeable zinc-ion batteries using potassium nickel hexacyanoferrate as a cathode material, J. Power Sources, 2017, 337, 204-211.
- 80 A. Zhou, L. Jiang, J. Yue, Y. Tong, Q. Zhang, Z. Lin, B. Liu, C. Wu, L. Suo, Y. S. Hu, H. Li and L. Chen, Water-in-Salt Electrolyte Promotes High-Capacity FeFe(CN)₆ Cathode for Aqueous Al-Ion Battery, ACS Appl. Mater. Interfaces, 2019, **11**(44), 41356-41362.
- 81 D. Wang, H. Lv, T. Hussain, Q. Yang, G. Liang, Y. Zhao, L. Ma, Q. Li, H. Li, B. Dong, T. Kaewmaraya and C. Zhi, A manganese hexacyanoferrate framework with enlarged ion tunnels and two-species redox reaction for aqueous Al-ion batteries, Nano Energy, 2021, 84, 105945.
- 82 S. Liu, G. L. Pan, G. R. Li and X. P. Gao, Copper hexacyanoferrate nanoparticles as cathode material for aqueous Al-ion batteries, J. Mater. Chem. A, 2015, 3(3), 959-962.
- 83 Y. Ru, S. Zheng, H. Xue and H. Pang, Potassium cobalt hexacyanoferrate nanocubic assemblies for highperformance aqueous aluminum ion batteries, Chem. Eng. J., 2020, 382, 122853.
- 84 X. Wu, J. J. Hong, W. Shin, L. Ma, T. Liu, X. Bi, Y. Yuan, Y. Qi, T. W. Surta, W. Huang, J. Neuefeind, T. Wu, P. A. Greaney, J. Lu and X. Ji, Diffusion-free Grotthuss topochemistry for high-rate and long-life proton batteries, Nat. Energy, 2019, 4(2), 123-130.
- 85 L. D. Reed, S. N. Ortiz, M. Xiong and E. J. Menke, A rechargeable aluminum-ion battery utilizing a copper hexacyanoferrate cathode in an organic electrolyte, Chem. Commun., 2015, 51(76), 14397-14400.
- 86 X. Zhang, G. Zhang, S. Wang, S. Li and S. Jiao, Porous CuO microsphere architectures as high-performance cathode materials for aluminum-ion batteries, J. Mater. Chem. A, 2018, 6(7), 3084-3090.
- 87 X. Xiao, M. Wang, J. Tu, Y. Luo and S. Jiao, Metal-Organic Framework-Derived Co₃O₄@MWCNTs Polyhedron as Cathode Material for a High-Performance Aluminum-Ion Battery, ACS Sustainable Chem. Eng., 2019, 7(19), 16200-16208.
- 88 T. Mori, Y. Orikasa, K. Nakanishi, C. Kezheng, M. Hattori, T. Ohta and Y. Uchimoto, Discharge/charge reaction mechanisms of FeS2 cathode material for aluminum rechargeable batteries at 55 °C, J. Power Sources, 2016, 313, 9-14.
- 89 Z. Yu, Z. Kang, Z. Hu, J. Lu, Z. Zhou and S. Jiao, Hexagonal NiS nanobelts as advanced cathode materials for

- rechargeable Al-ion batteries, Chem. Commun., 2016, 52(68), 10427-10430.
- 90 S. Wang, Z. Yu, J. Tu, J. Wang, D. Tian, Y. Liu and S. Jiao, A Novel Aluminum-Ion Battery: Al/AlCl₃-[EMIm]Cl/Ni₃S₂@-Graphene, Adv. Energy Mater., 2016, 6(13), 1600137.
- 91 J. Tu, M. Wang, X. Xiao, H. Lei and S. Jiao, Nickel Phosphide Nanosheets Supported on Reduced Graphene Oxide for Enhanced Aluminum-Ion Batteries, ACS Sustainable Chem. Eng., 2019, 7(6), 6004-6012.
- 92 S. Lu, M. Wang, F. Guo, J. Tu, A. Lv, Y. Chen and S. Jiao, Self-supporting and high-loading hierarchically porous Co-P cathode for advanced Al-ion battery, Chem. Eng. J., 2020, 389, 124370.
- 93 C. Li, S. Dong, P. Wang, C. Wang and L. Yin, Metal-Frameworks-Derived Tunnel Co₃(PO₄)₂@C as Cathode for New Generation High-Performance Al-Ion Batteries, Adv. Energy Mater., 2019, 9(41), 1902352.
- 94 T. Cai, L. Zhao, H. Hu, T. Li, X. Li, S. Guo, Y. Li, Q. Xue, W. Xing, Z. Yan and L. Wang, Stable CoSe₂/carbon nanodice@reduced graphene oxide composites for highperformance rechargeable aluminum-ion batteries, Energy Environ. Sci., 2018, 11(9), 2341-2347.
- 95 Y. Hu, D. Ye, B. Luo, H. Hu, X. Zhu, S. Wang, L. Li, S. Peng and L. Wang, A Binder-Free and Free-Standing Cobalt Sulfide@Carbon Nanotube Cathode Material for Aluminum-Ion Batteries, Adv. Mater., 2018, 30(2), 1703824.
- 96 Z. Hu, K. Zhi, Q. Li, Z. Zhao, H. Liang, X. Liu, J. Huang, C. Zhang, H. Li and X. Guo, Two-dimensionally porous cobalt sulfide nanosheets as a high-performance cathode for aluminum-ion batteries, J. Power Sources, 2019, 440, 227147.
- 97 R. Zhuang, Z. Huang, S. Wang, J. Qiao, J.-C. Wu and J. Yang, Binder-free cobalt sulfide@carbon nanofibers composite films as cathode for rechargeable aluminumion batteries, Chem. Eng. J., 2021, 409, 128235.
- 98 A. N. Buckley and R. Woods, Electrochemical and XPS studies of the surface oxidation of synthetic heazlewoodite (Ni₃S₂), J. Appl. Electrochem., 1991, 21(7), 575–582.
- 99 S. Wang, S. Jiao, J. Wang, H. S. Chen, D. Tian, H. Lei and D. N. Fang, High-Performance Aluminum-Ion Battery with CuS@C Microsphere Composite Cathode, ACS Nano, 2017, 11(1), 469-477.
- 100 B. Minceva-Sukarova, M. Najdoski, I. Grozdanov and C. J. Chunnilall, Raman spectra of thin solid films of some metal sulfides, J. Mol. Struct., 1997, 410-411, 267-270.
- 101 H. Hong, J. Liu, H. Huang, C. Atangana Etogo, X. Yang, B. Guan and L. Zhang, Ordered Macro-Microporous Metal-Organic Framework Single Crystals and Their Derivatives for Rechargeable Aluminum-Ion Batteries, J. Am. Chem. Soc., 2019, 141(37), 14764-14771.
- 102 X. Huang, Y. Liu, C. Liu, J. Zhang, O. Noonan and C. Yu, Rechargeable Aluminum-Selenium Batteries with High Capacity, Chem. Sci., 2018, 9(23), 5178-5182.
- 103 Z. Li, J. Liu, X. Huo, J. Li and F. Kang, Novel One-Dimensional Hollow Carbon Nanotubes/Selenium

- Composite for High-Performance Al-Se Batteries, ACS Appl. Mater. Interfaces, 2019, 11(49), 45709-45716.
- 104 S. Liu, X. Zhang, S. He, Y. Tang, J. Wang, B. Wang, S. Zhao, H. Su, Y. Ren, L. Zhang, J. Huang, H. Yu and K. Amine, An advanced high energy-efficiency rechargeable aluminumselenium battery, Nano Energy, 2019, 66, 104159.
- 105 T. Zhang, T. Cai, W. Xing, T. Li, B. Liang, H. Hu, L. Zhao, X. Li and Z. Yan, A rechargeable 6-electron Al-Se battery with high energy density, Energy Storage Mater., 2021, 41, 667-676.
- 106 W. Chu, X. Zhang, J. Wang, S. Zhao, S. Liu and H. Yu, A low-cost deep eutectic solvent electrolyte for rechargeable aluminum-sulfur battery, Energy Storage Mater., 2019, 22, 418-423.
- 107 H. Yang, L. Yin, J. Liang, Z. Sun, Y. Wang, H. Li, K. He, L. Ma, Z. Peng, S. Qiu, C. Sun, H. M. Cheng and F. Li, An Aluminum-Sulfur Battery with a Fast Kinetic Response, Angew. Chem., Int. Ed., 2018, 57(7), 1898–1902.
- 108 G. Cohn, L. Ma and L. A. Archer, A novel non-aqueous aluminum sulfur battery, I. Power Sources, 2015, 283, 416-422.
- 109 Y. Wang, J. Wu, Y. Tang, X. Lü, C. Yang, M. Qin, F. Huang, X. Li and X. Zhang, Phase-Controlled Synthesis of Cobalt Sulfides for Lithium Ion Batteries, ACS Appl. Mater. Interfaces, 2012, 4(8), 4246-4250.
- 110 S. Zheng, F. Yi, Z. Li, Y. Zhu, Y. Xu, C. Luo, J. Yang and C. Wang, Copper-Stabilized Sulfur-Microporous Carbon Cathodes for Li-S Batteries, Adv. Funct. Mater., 2014, 24(26), 4156-4163.
- 111 Y. Guo, H. Jin, Z. Qi, Z. Hu, H. Ji and L.-J. Wan, Carbonized-MOF as a Sulfur Host for Aluminum-Sulfur Batteries with Enhanced Capacity and Cycling Life, Adv. Funct. Mater., 2019, 29(7), 1807676.
- 112 Y. Guo, Z. Hu, J. Wang, Z. Peng, J. Zhu, H. Ji and L. J. Wan, Rechargeable Aluminium-Sulfur Battery with Improved

- Electrochemical Performance by Cobalt-Containing Electrocatalyst, Angew. Chem., Int. Ed., 2020, 59(51), 22963-22967.
- 113 H. Li, R. Meng, Y. Guo, B. Chen, Y. Jiao, C. Ye, Y. Long, A. Tadich, Q. H. Yang, M. Jaroniec and S. Z. Qiao, Reversible electrochemical oxidation of sulfur in ionic liquid for highvoltage Al-S batteries, Nat. Commun., 2021, 12(1), 5714.
- 114 L. Yao, S. Ju, T. Xu and X. Yu, Spatial Isolation-Inspired Ultrafine CoSe₂ for High-Energy Aluminum Batteries with Improved Rate Cyclability, ACS Nano, 2021, 15(8), 13662–13673.
- 115 J. Li, W. Liu, Z. Yu, J. Deng, S. Zhong, Q. Xiao, F. chen and D. Yan, N-doped C@ZnSe as a low cost positive electrode for aluminum-ion batteries: Better electrochemical performance with high voltage platform of ~1.8 V and new reaction mechanism, Electrochim. Acta, 2021, 370, 137790.
- 116 N. S. Hudak, Chloraluminate-Doped Conducting Polymers as Positive Electrodes in Rechareable Aluminum Batteries, J. Phys. Chem. C, 2014, 118, 5203-5215.
- 117 D. J. Kim, D.-J. Yoo, M. T. Otley, A. Prokofjevs, C. Pezzato, M. Owczarek, S. J. Lee, J. W. Choi and J. F. Stoddart, Rechargeable aluminium organic batteries, Nat. Energy, 2018, 4(1), 51-59.
- 118 J. Zhou, X. Yu, J. Zhou and B. Lu, Polyimide/metal-organic framework hybrid for high performance Al - Organic battery, Energy Storage Mater., 2020, 31, 58-63.
- 119 J. Bitenc, N. Lindahl, A. Vizintin, M. E. Abdelhamid, R. Dominko and P. Johansson, Concept and electrochemical mechanism of an Al metal anode - organic cathode battery, Energy Storage Mater., 2020, 24, 379-383.
- 120 D. J. Yoo, M. Heeney, F. Glocklhofer and J. W. Choi, Tetradiketone macrocycle for divalent aluminium ion batteries, Nat. Commun., 2021, 12(1), 2386.
- 121 X. Yu and A. Manthiram, Electrochemical Energy Storage with a Reversible Nonaqueous Room-Temperature Aluminum-Sulfur Chemistry, Adv. Energy Mater., 2017, 7(18), 1700561.